CARBON SUPPORTED AND SURFACTANT STABILIZED METAL NANOPARTICLE CATALYSTS FOR DIRECT METHANOL FUEL CELLS

A THESIS SUBMITTED TO
THE GRADUATE SCHOOL OF NATURAL AND APPLIED SCIENCES
OF
MIDDLE EAST TECHNICAL UNIVERSITY

BY

ÇAĞLAR ÇELİK

IN PARTIAL FULFILLMENT OF THE REQUIREMENTS
FOR
THE DEGREE OF MASTER OF SCIENCE
IN
DEPARTMENT OF CHEMISTRY

AUGUST 2005

Approval of the Graduate School of Natural and Applied Sciences

Prof. Dr. Canan Özgen
Director

I certify that this thesis satisfies all the requirements as a thesis for the degree of Master of Science.

Prof. Dr. Hüseyin İşçi
Head of Department

This is to certify that we have read this thesis and that in our opinion it is fully adequate, in scope and quality, as a thesis for the degree of Master of Science.

Assoc. Prof. Dr. Gülsün Gökağaç
Supervisor

Examining Committee Members

Prof. Dr. Hüseyin İşçi (METU,CHEM)

Assoc. Prof. Dr. Gülsün Gökağaç (METU, CHEM)

Prof. Dr. Raşit Turan (METU, PHYSICS)

Asst. Prof. Dr. Michael Pitcher (METU, CHEM)

Asst. Prof. Dr. Ayşen Yılmaz (METU CHEM)

I hereby declare that all information in this document has been obtained and presented in accordance with academic rules and ethical conduct. I also declare that, as required by these rules and conduct, I have fully cited and referenced all material and results that are not original to this work.

Name, Last name : Çağlar ÇELİK

Signature :

ABSTRACT

CARBON SUPPORTED AND SURFACTANT STABILIZED METAL NANOPARTICLE CATALYSTS FOR DIRECT METHANOL FUEL CELLS

Çelik, Çağlar
M.S., Department of Chemistry
Supervisor: Assoc. Prof. Dr. Gülsün Gökağaç

August 2005, 72 pages

Carbon supported surfactant, such as 1-decanethiol and octadecanethiol, stabilized platinum and platinum/ruthenium species have been prepared recently. In this thesis, for the first time, 1-hexanethiol has been used as an organic stabilizer for the preparation of carbon supported platinum and platinum/ruthenium nanoparticle catalysts. These new catalysts were employed for methanol oxidation reaction, which were used for direct methanol fuel cells. Cyclic voltammetry, X-ray photoelectron spectroscopy and transmission electron microscopy have been used in order to determine the nature of the catalysts.

The effect of temperature and time on catalytic activity of catalysts were examined and the maximum catalytic activity was observed for carbon supported 1-hexanethiol stabilized platinum nanoparticle catalyst (with 1:1 thiol/platinum molar ratio) which was heated up at 200^{o}C for 5 hours. The particle size of platinum nanoparticles was determined to be ~ 10 nm in diameter.

The size and distribution of metal nanoparticles on carbon support, the Pt/Ru surface composition, the relative amount of Pt(0), Pt(II) and Pt(IV) and the removal

of organic surfactant molecules around the metal nanoparticles were found to be important in determining the catalytic activity of electrodes towards methanol oxidation reaction.

A significant decrease in catalytic activity was observed for carbon supported 1-hexanethiol stabilized $Pt_{75}Ru_{25}$ and $Pt_{97}Ru_3$ (with 1:1 thiol/PtRu molar ratio) with respect to carbon supported 1-hexanethiol stabilized Pt (with 1:1 thiol/platinum molar ratio). This result might be due to unremoved stabilizer shell around platinum/ruthenium nanoparticles and increase in amount of Pt(II) and Pt(IV) compared to Pt(0) where the methanol oxidation occured.

Keywords: Direct Methanol Fuel Cells, Platinum and Platinum-Ruthenium Nanoparticles, Carbon-Supported Thiol Stabilized Catalysts, Cyclic Voltammetry, Transmission Electron Microscopy, X-ray Photoelectron Spectroscopy.

ÖZ

DOĞRUDAN METANOL YAKIT PİLLERİ İÇİN KARBON DESTEKLİ VE SÜRFAKTANTLA STABİLİZE EDİLMİŞ METAL NANOKATALİZÖRLERİN HAZIRLANMASI VE ANALİZİ

Çelik, Çağlar
Yüksek Lisans, Kimya Bölümü
Tez Yöneticisi: Doç. Dr. Gülsün Gökağaç

Ağustos 2005, 72 sayfa

Son yıllarda, karbon destekli sürfaktantlar, örneğin 1-dekantiol, oktadekantiol, ile stabilize edilmiş platin ve platin/rutenyum maddeleri üzerinde çalışmalar yapılmıştır. Bu tez çalışmasında ilk kez 1-hegzantiol organik stabilizatörü kullanılarak, karbon destekli ve bu sürfaktantla stabilize edilmiş platin ve platin/rutenyum nanoparçacık katalizörleri hazırlanmıştır. Bu yeni katalizörler, doğrudan metanol yakıt pili sisteminde kullanılan metanolün yükseltgenme tepkimesinde kullanılmışlardır. Hazırlanan katalizörlerin doğasının aydınlatılmasında dönüşümlü voltametre, X-ışınları fotoelektron spektroskopisi ve transmisyon (geçirmeli) elektron mikroskopu tekniklerinden faydalanılmıştır.

Sıcaklığın ve zamanın katalitik aktiviteye olan etkisi incelenmiş ve en aktif katalizörün, karbon destekli, 1-hegzantiol ile stabilize edilmiş ve 200^{o}C'de 5 saat ısıtılmış olan platin nanoparçacık içeren katalizör olduğu bulunmuştur. Platin nanoparçacıkların çapı ~ 10 nm olarak ölçülmüştür.

Metal nanoparçacıkların boyutlarının ve karbon destek üzerindeki dağılımlarının, Pt/Ru yüzey kompozisyonunun, Pt(0), Pt(II) ve Pt(IV) türlerinin bağıl değerlerinin, sürfaktantların metal nanoparçacık yüzeyinden uzaklaşıp uzaklaşmamalarının hazırlanan maddelerin katalitik aktiviteleri üzerinde oynadığı rol saptanmıştır.

Hazırlanan karbon destekli 1-hegzantiol ile stabilize edilmiş $Pt_{75}Ru_{25}$ ve $Pt_{97}Ru_3$ nanoparçacık içeren katalizörlerin aktivitelerinin, karbon destekli 1-hegzantiol ile stabilize edilmiş Pt nanoparçacık içeren katalizörün aktivitesinden oldukça düşük olduğu gözlenmiştir. Bunun nedeni, stabilizatör tabakasının metal etrafından yeterince uzaklaştırılamamasıyla ve Pt(II) ve Pt(IV) miktarlarının metanol yükseltgenmesinde etkin tür olan Pt(0) miktarına göre artmasıyla açıklanabilir.

Anahtar Kelimeler: Doğrudan Methanol Yakıt Pilleri, Platin ve Platin-Rutenyum Nanoparçacıkları, Karbon Destekli ve Tiol ile Stabilize Edilmiş Katalizörler, Dönüşümlü Voltametre, Transmisyon (Geçirmeli) Elektron Mikroskopisi, X-ışınları Fotoelektron Spektroskopisi.

To My Family

ACKNOWLEDGMENTS

First, I would like to express my sincere thanks to Assoc. Prof. Dr. Gülsün Gökağaç for her continous interest, help, support and patience.

My special thanks go to Gökhan Bayar for his great support, trust, patience and love. This work couldn't be accomplished without him. He was always with me when I was in difficulty.

I'm grateful to my parents for their endless love, support, trust and encouragement.

I would like to thank my lab-mates Yasemin Özdil, Seher Karabıçak and Fatih Şen and also METU Chemistry Department for their sincere support during my M.S. study.

Lastly, I would like to thank the staff of central laboratory of METU (particularly Selda Keskin), METU Metallurgy Engineering Department, Kırıkkale University and Ankara University - İbni Sina Hospital for their help during my characterization studies.

TABLE OF CONTENTS

LIST OF TABLES

TABLES

LIST OF FIGURES

FIGURES

CHAPTER I

INTRODUCTION

1.1. FUEL CELLS AND THEIR ADVANTAGES

The form of energy most frequently required by man is electricity. The conventional methods, apart from hydroelectric power generation, pass through the intermediate stage of conversion of heat energy into mechanical energy which causes the loss of efficiency. Direct methods of energy conversion are preferred because of their simplicity, reliability and lessened weight and volume. Energy loss is prevented if the conversion of energy from a primary source to electricity can be made in one step. Fuel cells are better systems in this respect.

The first investigator, who successfully operated a fuel cell, was Sir William Groove in 1839 (Groove, 1839). He discovered the basic operating principle of fuel cells by reversing water electrolysis to generate electricity from hydrogen and oxygen. The principle that he discovered remains unchanged today: "*A fuel cell is an electrochemical 'device' that continuously converts chemical energy into electrical energy (and some heat) for as long as fuel and oxidant are supplied* ".

The fuel cells consist of two electrodes: (a) the anode, where the fuel (typically hydrogen, methanol or hydrazine) is oxidized, and (b) the cathode, where the reduction (usually of molecular oxygen) takes place. The basic advantages of fuel cells are:

(i) EFFICIENCY

Chemical energy is converted directly into electricity in fuel cells without a preliminary conversion into heat and no mechanical conversion is required such as boiler-to-turbine and turbine-to-generator systems. Although 100% efficiency is possible from fuel cells, in practice, 50% or greater efficiency is observed with current technology.

(ii) MANIFACTURING

The manifacturing cost of fuel cell is low as compared to engines, where close tolerances are required. There are no moving parts in a cell, hence sealing problems are minimum and no bearing problems exist. Fuel and manifolds and diffusers can be punched, pressed, or cast in metal or plastic.

(iii) MAINTENANCE

Because there are no moving parts, most fuel cells present little or no maintenance problems. Wear or tear, aging, corrosion, etc., are no more aggravated in fuel cells than in comparable battery systems. In high temperature cells corrosion is still a serious problem; in low temperature cells is less worrisome. Fuel cells can provide long, trouble-free life.

(iv) WEIGHT AND VOLUME

Performance of power units or systems is often defined in terms of power-per-unit-volume and power-per-unit-weight. When compared with batteries and engine generator sets, fuel cells are the most advantageous ones in terms of performance.

(v) NOISE

Because they have no moving parts, the cells provide silent electrical power. Also, with suitable solid state components, alternating current devoid of all electrical noise can be provided at high efficiency. This property is a big advantage in military and communication applications.

(vi) HEAT

The electrical efficiencies in a fuel cell may be manifested as heat; however, with proper design of a cell, efficiency can be maximized and heat can be minimized. A military advantage of the low temperature cell is the minimized detectable heat loss.

(vii) CLEANLINESS

In most fuel cells under consideration today for practical application there are no noxious fumes or other objectionable combustion products. End products are usually water, carbon dioxide, or nitrogen. Unused fuels and oxidants can be recirculated and electrolytes are totally enclosed or isolated from exhaust systems.

(viii) CAPACITY

In addition to providing direct current, one of the major advantages of fuel cells for mobile power is their high overload capacity. The power systems are in general to stand brief overloads of 100% or more. Thus, the rating of a fuel cell can be much lower for a vehicle than that of an internal combustion engine which must be rated for the peak demand. The only factor affected by briefly overloading a cell is efficiency.

(ix) RELIABILITY

Although many types of systems are not highly refined at the present time, it is known from experience with the hydrogen-oxygen cell that the device has a potential reliability equivalent to the storage battery as its best. Without this reliability, fuel cells obviously could not be considered for use in manned space vehicles.

1.2. THE HISTORY OF FUEL CELLS

The idea of fuel cells is not a new one. Sir William Grove, in 1839, was the first to observe that when hydrogen and oxygen were supplied separately to two platinum electrodes immersed in sulfuric acid, a current was produced in the external circuit connecting the two platinum electrodes through a load (Grove, 1839). The term fuel cells was only coined 50 years later by Mond and Langer, who somewhat improved Grove's hydrogen-oxygen fuel cells (Mond and Langer, 1889). William Ostwald realized the great potentialities of fuel cells – for example, the possibility of obtaininig high thermal efficiencies (Ostwald, 1894). Ostwald also conceived the idea of using carbon as the fuel with oxygen or air as the oxidizing agent. This idea was taken by Jacques who built a 1.5 kW fuel cell battery using a carbon rod as the anode material (Jacques, 1897). The electrolyte was fused sodium hydroxide. Haber and Brünner interpreted that Jacques' cell was actually a hydrogen-oxygen cell in the sense that hydrogen was produced by the chemical reaction of carbon with sodium

hydroxide (Haber and Brünner, 1904 and 1906). Baur and others worked on coal-based fuel cells (Baur and Preis, 1937). The pioneer of the modern phase in fuel cell research is F. T. Bacon (Bacon, 1960). He started working in the thirties to develop a hydrogen-oxygen fuel using cheap catalysts (nickel anode and lithiated nickel oxide cathode) which operates at moderate temperatures (200 to 204^{o}C) and pressures (30 to 40 atm) using an alkaline electrolyte. It was fully developed into a multikilowatt generator by 1952. Davytan researched on molten carbonate electrolyte fuel cells which operate at temperatures of over 500^{o}C using hydrogen or carbon monoxide as fuels (Davytan, 1946). Similar work was commenced in the early fifties by Ketelaar and Broers (Ketelaar and Broers, 1960).

In 1970, K. Kordesch built a hydrogen fuel cell/battery hybrid vehicle for 4 passengers, which was operated for 3 years in city traffic. The mid-1970s showed an interesting change in the direction of fuel cell technology. The alkaline system, which had reached the highest level of development in the space programs, was replaced in the world-wide research and development efforts by the phosphoric-acid system, which was seemingly better suited for stationary power plants. Parallel to these efforts, the development of reformers became necessary as hydrocarbons would be the preferred fuels. This trend to large-scale power plants was especially noticeable in Japan after a loss of interest in the USA. Power plants in the 50-100 kW and up to 10 Megawatt sizes achieved acceptable lifetimes for prototypes.

However, due to their obviously better overall efficiency together with the heat from a high temperature plant, the development of molten carbonate fuel cell systems in the 1980s and of solid oxide fuel cells in the 1990s accelerated. Unfortunately, the life expectancy problems have still to be solved for the high temperature fuel cells.

Another surprising turn in technology occurred in the 1990s. The membrane fuel cell system appeared as the most active object for development. This system was already in existence in the 1960s, but did not perform reliable in the space fuel cell projects and its importance fell behind the alkaline systems. High power densities were obtained as a result of new membrane types and catalyst research. Operating life expectancies improved also considerably. One large draw-back remained; that is

the high cost of the membranes and the expensive auxiliary system for heat and water removal.

1.3. MAIN APPLICATIONS OF FUEL CELLS

It was not until the beginnings of space travel that fuel cells saw their first practical application in generating electric power (and drinking water) in the Gemini and Apollo programs. Extensive research efforts were made in those days, and many results from that work are still perfectly valid and have been incorporated into modern fuel cell systems; others continue to inspire modern-day researchers. In the near future, fuel cells will eventually come into widespread commercial use, through three main applications: transportation, stationary power generation, and portable applications.

1.3.1. TRANSPORTATION

In the transportation sector, fuel cells are probably the most serious contenders to compete with internal combustion engines (ICEs). They are highly efficient because they are electrochemical rather than thermal engines. Hence, they can help to reduce the consumption of primary energy and the emission of SO_2, NO_x, CO_2. This is what mainly inspired automotive companies and other fuel cell developers in 1980s and 1990s to start developing fuel-cell-powered cars and buses (Hoogers, 2003).

1.3.2. STATIONARY POWER

Stationary power generation is viewed as the leading market for fuel cell technology other than buses. In fact, fuel cells are currently the only practical engines for micro-CHP (combined heat and power generation) systems in the domestic environment (5-10 kW). They can also be used as great power sources, for example

so far several hundred 200-kW phosphoric acid fuel cell plants has been installed worldwide (Hoogers, 2003).

1.3.3. PORTABLE POWER

The term "portable fuel cells" often includes grid-independent applications such as camping, yachting, and traffic monitoring. It is believed that fuel cells will be widely used in personal electronics as primary power or battery charging for cell phones, laptops, PDAs, cameras, MP3 players, etc. in the near future (Hoogers, 2003).

1.4. TYPES OF FUEL CELLS

A whole family of fuel cells that now exists can be characterized by the electrolyte they use and by a related acronym (Table 1.1.). All of these fuel cells function in the same basic way: at the anode, a fuel is oxidized into electrons and protons, and at the cathode, oxygen is reduced to oxide species. Depending on the electrolyte, either protons or oxide ions are transported through the ion-conducting but electronically insulating electrolyte to combine with oxide or protons to generate water and electric power.

1.5. THE DIRECT METHANOL FUEL CELL

It is appearent that there are large number of different fuel cells, some of which may be optimised for particular applications. However, the direct methanol fuel cell, DMFC, appears favorable for small scale power generation, <15 kW, such as road transport and portable generators (Weeks, 1988). Specific advantages of the DMFC include:

Table 1.1. Currently developed types of fuel cells and their characteristics and applications.

Fuel Cell Type	Electrolyte	Charge Carrier	Operating Temperature	Fuel	Electric Efficiency (System)	Power Range/Application
Alkaline Fuel Cell (AFC)	KOH	OH^-	60-120°C	Pure H_2	35-55%	< 5 kW, niche markets (military, space)
Proton Exchange Membrane Fuel Cell (PEMFC)	Solid polymer (such as nafion)	H^+	50-100°C	Pure H_2 (tolerates CO_2), Methanol [in Direct Methanol Fuel Cell (DMFC)]	35-45%	Automotive, CHP (5-250 kW), portable
Phosphoric Acid Fuel Cell (PAFC)	H_3PO_4	H^+	~220°C	Pure H_2 (tolerates CO_2, approx. 1% CO)	40%	CHP (200 kW)
Molten Carbonate Fuel Cell (MCFC)	Li_2CO_3 and K_2CO_3	CO_3^{2-}	~650°C	H_2, CO, CH_4, other hydrocarbons (tolerates CO_2)	>50%	200 kW-MW range, CHP and stand-alone
Solid Oxide Fuel Cell (SOFC)	Solid oxide electrolyte (yttria, zirconia)	O^{2-}	~1000°C	H_2, CO, CH_4, other hydrocarbons (tolerates CO_2)	>50%	2 kW-MW range, CHP and stand-alone

(a) Methanol is readily available from coal, natural gas, wood and municipal or agricultural waste.

(b) Methanol is cheap in comparison to other hydrocarbons.

(c) Although methanol has a lower electro-activity in acid solutions than formaldehyde or formic acid (Schlatter, 1963; Vielstich, 1970a and b), it is a better fuel because of its potentially higher energy content per unit mass (Liebhavskky and Cairns, 1968; Cathro and Weeks, 1971).

(d) High efficiencies of fuel cells compared to internal combustion engines result in a more environmentally acceptible power source. Also the lack of sulfur and nitrogen additives in the fuel means there is no SO_2 or NO_x production. This makes methanol an environmentally better fuel than any petroleum product, natural or synthetic.

(e) Methanol is a liquid fuel, therefore it is easier to store and transport than gaseous fuels such as hydrogen.

(f) Methanol is oxidized at room temperaures, which would make it suitable for use in cars and other vehicles (Mcnicol, 1981).

(g) Methanol is soluble in aqueous media, which allows a wide range of solvents to be used.

(h) The DMFC is relatively low weight compared to the internal combustion engine or conventional storage batteries. It is small enough to serve as an automobile engine (Mcnicol, 1981).

(i) There are few moving parts in a DMFC, thus decreasing the chance of mechanical failure, leading to reduced maintenance and simplicity of working.

(j) If a cheap electro-oxidative catalyst can be found for methanol then it will be more reactive under acidic conditions than many other fuels.

1.5.1. OPERATING PRINCIPLE OF THE DMFC

A schematic of a DMFC employing an acidic solid polymer electrolyte membrane is shown in Figure 1.1. Methanol and water electrochemically react (i.e., methanol is electro-oxidized) at the anode to produce carbon dioxide, protons and electrons as shown in Equation 1.1. An acidic electrolyte is advantageous to aid CO_2 rejection since insoluble carbonates form in alkaline electrolytes. The reaction for methanol oxidation in alkaline solution is (Hamnett et al., 1987):

$$CH_3OH + 8OH^- \rightarrow CO_3^{2-} + 6H_2O + 6e^-$$

The protons produced at the anode migrate through the polymer electrolyte to the cathode where they can react with oxygen (usually from air) to produce water as shown in Equation 1.2. The electrons produced at the anode carry the free energy change of the chemical reaction and travel through the external circuit where they can be made to do useful work, such as powering an electric motor.

Anode reaction:

$CH_3OH + H_2O \rightarrow CO_2 + 6H^+ + 6e^-$ $E^o = 0.043$ V * (vs. SHE$^\#$)

(1.1)

Cathode reaction:

$3/2\ O_2 + 6H^+ + 6e^- \rightarrow 3\ H_2O$ $E^o = 1.229$ V * (vs. SHE$^\#$)

(1.2)

Overall reaction:

$CH_3OH + 3/2\ O_2 \rightarrow CO_2 + 2H_2O$ $E^o = 1.186$ V * (vs. SHE$^\#$)

(1.3)

* These are theoretical E^o values calculated from thermodynamic data.

$^\#$ Standart hydrogen electrode.

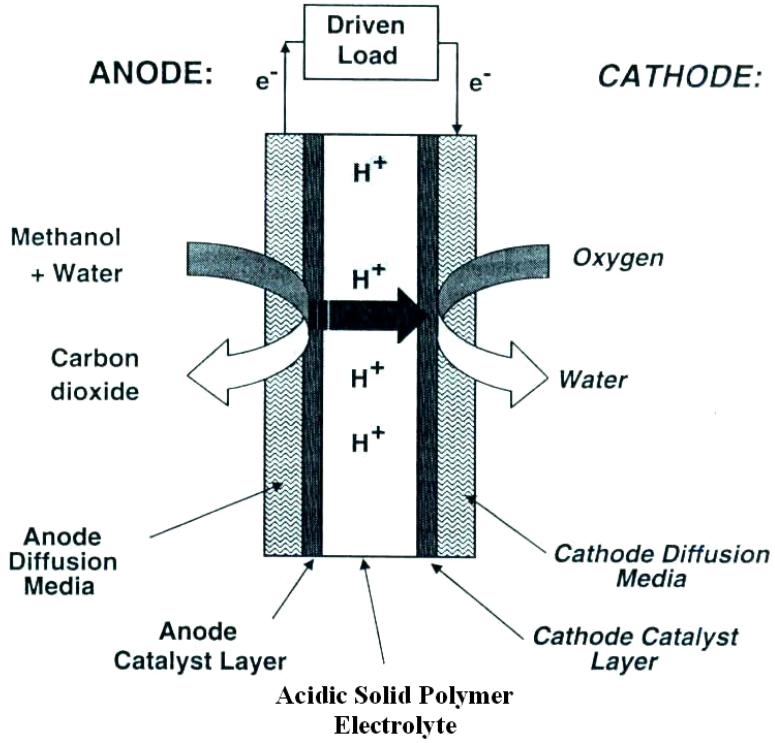

Figure 1.1. Schematic of a DMFC employing an acidic solid polymer electrolyte membrane.

1.5.2. THE NEED FOR A CATALYST

Although methanol has a lot of adventages to use in direct methanol fuel cells, it has poor electrochemical reactivity in acid solutions, which limits its use for practical purposes. Consequently, a catalyst is neeeded to activate the methanol. The active electrocatalysts in acid medium (to reject the produced CO_2) are platinum-group metals, in particular Pt itself (Bockris and Srinivasan, 1969; McNicol, 1978; Bockris et al., 1981). The high cost and rapid poisoning of platinum metal has motivated researchers to find an alternative affordable catalyst. In order to solve this problem, the mechanism of the electrooxidation of methanol in aqueous solution has been extensively studied over the last four decades (Williams, 1966; Bockris and Srinivasan, 1969).

1.5.3. THE MECHANISM OF METHANOL ELECTROOXIDATION ON PLATINUM IN ACID SOLUTIONS

Anodic reaction of a DMFC is a complex reaction involving the transfer of six electrons per molecule. Intermediate reactive species and poisoning species take part in the reaction mechanism, so that the electrocatalysis of such a reaction is difficult. As seen in Figure 1.2., the mechanism of methanol electrooxidation reaction involves two competing reactions: one is the oxidation of methanol, the other is the poisoning of the platinum catalyst. In the oxidation mechanism of methanol, it is generally believed that the adsorption of methanol on platinum surface occurs between 0.2 V and 0.5 V (vs SHE) which was verified by both electrochemical and radioactive tracer (^{14}C) methods (Kazarinov et al., 1975). It has been pointed out that in order to complete methanol oxidation reaction, the oxidation of adsorbed organic fragments, Pt_3COH, with OH_{ads}, which come from the electrosorption of water molecules, is needed:

$$H_2O \leftrightarrow H_2O_{ads} \quad (1.4)$$

$$H_2O_{ads} \leftrightarrow OH_{ads} + H^+ + e^- \quad (1.5)$$

However, reaction 1.5 can only occur at a potential greater than the potential at which methanol begins to be oxidized, 0.5 V (vs SHE). It is therefore argued that the oxygen containing species involved in the surface reaction is not OH_{ads} but adsorbed water molecules strained as a consequence of bonding with the platinum surface. Such strained molecules are reactive in methanol oxidation region (Biegler, 1973). It is also noted that at potentials higher than 0.85 V (vs SHE), the rate of methanol oxidation decreases (Bagotzky and Vassiliev, 1967; Biegler and Koch, 1967; Bagotzky et al., 1977; Hampson and Willars, 1979; McNicol,1981), due to the formation of a platinum oxide layer. It is usually accepted that the reaction between Pt_3–COH and $Pt–OH_{2(ads)}$ is the rate limiting step in the electrooxidation of methanol at lower potentials.

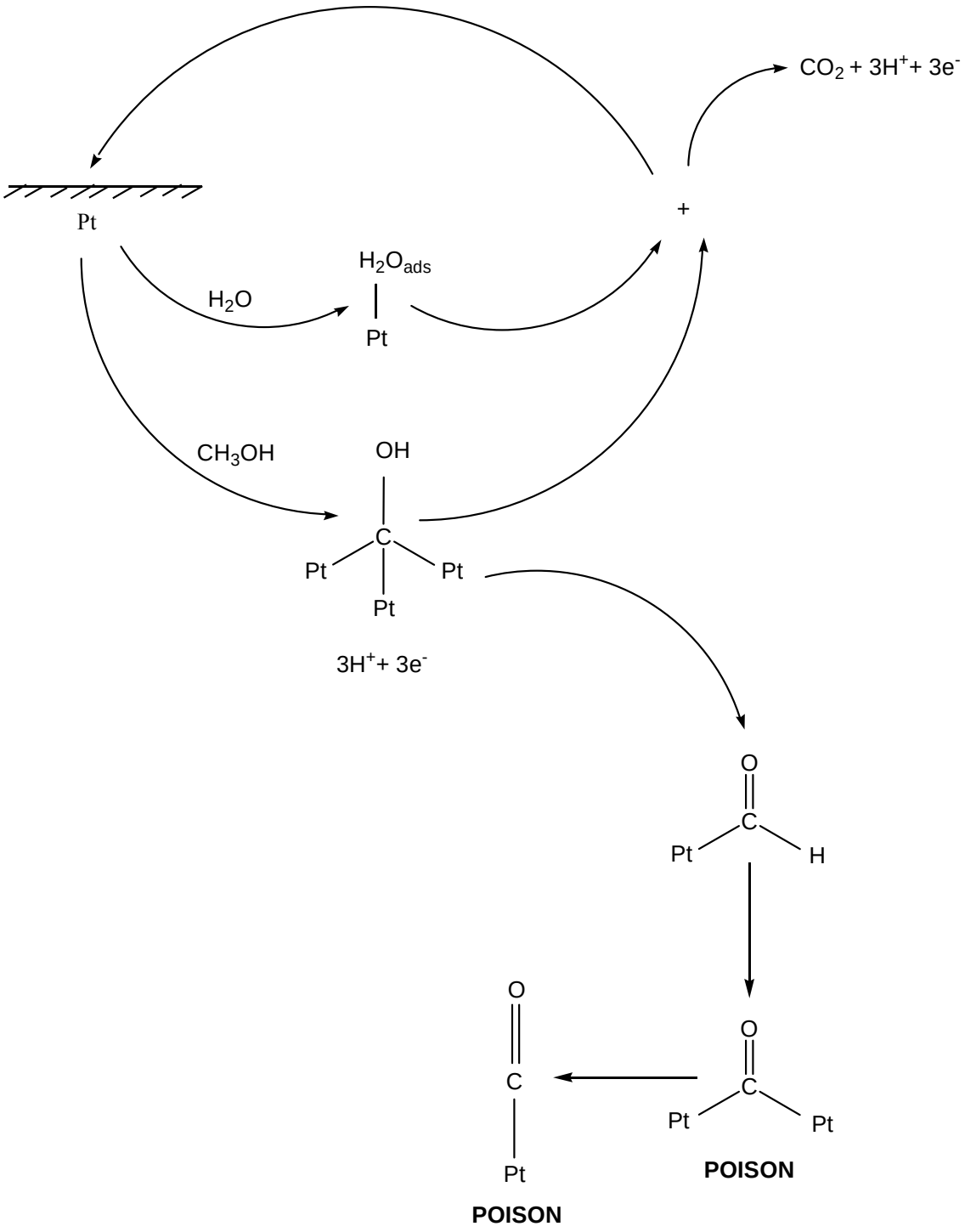

Figure 1.2. Schematic diagram of methanol oxidation occuring on the surface of a platinum catalyst. Two competing reactions occuring: (a) oxidation of methanol and (b) the poisoning of the platinum catalyst.

1.5.4. ACTIVITY OF PLATINUM-SECOND METAL CATALYSTS

It is well established that the catalytic activity of platinum for the electrooxidation of methanol to carbon dioxide at low temperatures can be enhanced by the addition of a promoter such as Ru, Rh, or Ti either by alloying or electro-deposition (McNicol, 1981; Beden et al. 1981; Hamnett et al., 1990). Three possible mechanisms by which the promoters may work have been postulated:

(a) The enhanced behaviour is due to the direct reaction of an oxide of the second metal, such as Ru, with the chemisorbed Pt_3COH residue, yielding CO_2 (Watanabe and Motoo, 1975). The metal oxide is regenerated via a second redox process.

(b) The enhanced performance of the bimetallic electrode is due to a blocking effect of the second metal, for example Pb, which is assumed to inhibit poison formation on the surface of the electrode (Adzic, 1979).

(c) Finally, there is the promoter model which appears appropriate for Ti and Sn, where the second metal promotes the formation of active platinum oxide groups capable of completing the oxidation reaction (Katayama, 1980; Hamnett and Kennedy, 1988).

Pt + Ru is generally taken to be the most active binary catalyst, with increases in methanol oxidation current up to ten times over that of pure platinum (Watanabe and Motoo, 1975; McNicol and Short, 1977). However, it is noted that many of these bimetallic systems are electrochemically unstable, the second metal dissolving into solution at higher potentials particularly under potentiodynamic cycling conditions, (Beden et al., 1981) and have not enough activity to use in practical purposes.

1.6. THE AIM OF STUDY

It is generally accepted that alloy formation or deposition of second metal, such as Ru, on the platinum metal, increase in active surface area of metals by supported materials, such as carbon, and oxidation state of metals are important parameters on the performance of catalysts for methanol oxidation reaction. Enormous studies have been performed to determine these factors and to characterize these alloys and surface modified systems, whilst relatively few studies have been reported for carbon supported platinum and platinum-second metal nanoparticle catalysts. It is well known that nanoparticles, <100 nm, have became a subject of great interest nowadays, as in catalyst applications because of active surface area relative to total volume, which makes them attractive for product development. Metal nanoparticles are widely used as catalysts, since the catalytic activities of metals are strongly dependent on the metal particles' sizes and their distributions on the supported materials.

Until now different types of stabilizers, such as 1-decanethiol and 1-octadecanethiol have been used for the preparation of metal nanoparticles. In the present work, for the first time, 1-hexanethiol has been used in order to prepare platinum and platinum/ruthenium nanoparticles and those nanoparticles dispersed on carbon support. The performance of these newly prepared catalysts were examined for methanol oxidation reaction and characterized by TEM, XPS, cyclic voltammetry and XRD. The temperature and time effect on catalytic activity of these catalysts towards methanol oxidation reaction were also studied.

CHAPTER II

EXPERIMENTAL

2.1. CATALYST PREPARATIONS

2.1.1. PREPARATION OF 1-HEXANETHIOL STABILIZED PLATINUM NANOPARTICLE CATALYST WITH 1:1 THIOL/PLATINUM MOLAR RATIO

1.0 mmol (0.3371g) of $PtCl_4$ (99%, Alfa) was dissolved in 20 ml of anhydrous tetrahydrofuran (THF, 99.5%, Merck) for an hour. Then 1.0 mmol (149 μL) of 1-hexanethiol surfactant ($C_6H_{13}SH$, 95%, Merck) was added to this solution and the mixture was stirred vigorously for 2.5 hours. Finally, thiol stabilized platinum complex was reduced by dropwise addition of lithium triethylborohydride (superhydride, 1.0 M dissolved in THF, Aldrich). Superhydride addition continued until no H_2 gas bubbled upon the solution according to Equation 2.1. All of these steps were performed under high-purity argon atmosphere. The observation of reddish-brown color of the solution indicated the formation of platinum nanoparticles (Yee et al.1999).

To remove the excess thiols, the resulting solution was washed with 400 ml of dry ethanol (99.9%, Merck) in an ultrasonic bath and then the solution was cooled to -18

^{o}C to have most of the particles precipitated (Brust et al., 1994). This process was continued until a clear filtrate solution was obtained. Finally, the solid residue was dried under vacuum at room temperature.

$PtCl_4$-surfactant + $LiBEt_3H \rightarrow$ Pt(nanoparticles)-surfactant + BEt_3 + LiCl + $H_2\uparrow$ (2.1.)

2.1.2. PREPARATION OF 1-HEXANETHIOL STABILIZED RUTHENIUM NANOPARTICLE CATALYST WITH 1:1 THIOL/RUTHENIUM MOLAR RATIO

Appropriate amount of $RuCl_3.0.5H_2O$ (Sigma) was used as a starting material instead of $PtCl_4$ and the same procedure was followed as in Section 2.1.1. In this case, the observation of dark brown solution instead of reddish brown indicated the formation of ruthenium nanoparticles.

2.1.3. PREPARATION OF 1-HEXANETHIOL STABILIZED $Pt_{75}Ru_{25}$ NANOPARTICLE CATALYST WITH 1:1 THIOL/PtRu MOLAR RATIO

0.5 mmol (0.1685 g) of $PtCl_4$ and 0.5 mmol (0.1082 g) of $RuCl_3.0.5H_2O$ were taken and dissolved together in 20 ml of anhydrous THF, and then the same procedure in Section 2.1.1. was followed. The color of the solution was dark brown which indicated the formation of PtRu nanoparticles. Experimentally, the Pt/Ru atomic ratio was taken to be 50/50, however, the surface atomic ratio was found to be 75/25 by XPS. Therefore, this atomic ratio was used throughout the thesis.

2.1.4. PREPARATION OF 1-HEXANETHIOL STABILIZED $Pt_{97}Ru_3$ NANOPARTICLE CATALYST WITH 1:1 THIOL/PtRu MOLAR RATIO

0.9 mmol (0.3034g) of $PtCl_4$ and 0.1 mmol (0.0216g) of $RuCl_3.0.5H_2O$ were taken and dissolved together in 20 ml of anhydrous THF. And then the same procedure in Section 2.1.1. was followed (at the end of synthesis, the observation of dark-brown solution indicated the formation of PtRu nanoparticles). The surface Pt/Ru atomic ratio was found to be 97 to 3 ($Pt_{97}Ru_3$) by XPS, and used throughout the thesis.

2.1.5. PREPARATION OF CARBON SUPPORTED METAL (Pt, Ru AND Pt/Ru) NANOPARTICLE CATALYSTS

As synthesized Pt, Ru or PtRu nanoparticle catalyst was mixed with Cabot Vulcan XC-72 carbon (10 wt% nanoparticle) (Liu et al., 2004) and 10 ml of dry ethanol was added to the mixture and it was stirred vigorously overnight in order to obtain uniform distribution of metal nanoparticles on carbon support. Then, the slurry mixture was cooled to -18 ^oC until all the particles had been precipitated. Finally, the solution above the solid part was discarded and the solid residue was dried at room temperature under vacuum.

2.2. HEAT-TREATMENT EXPERIMENTS

The stabilizing surfactant shell around the metal nanoparticles had to be removed before they could be used as electrocatalysts (Liu et al., 2004), because platinum acts as a main catalyst towards methanol electrooxidation reaction. For this purpose, synthesized carbon supported surfactant stabilized Pt nanoparticle catalysts were heat-treated under argon atmosphere at different temperatures (between 100 to 400^oC by rising 50 ^oC in each step) and time intervals (2 - 5 -10 and 20 h at each temperature) in

order to define the optimum heating temperature and time for high performance of methanol electrooxidation reaction, Table 2.1.

Table 2.1. Heat-treatment experiments for carbon supported 1-hexanethiol stabilized Pt nanoparticle catalyst.

Time (h) / Temp. (^{o}C)	2	5	10	20
100	✓	✓	✓	✓
150	✓	✓	✓	✓
200	✓	✓	✓	✓
250	✓	✓	✓	✓
300	✓	✓	✓	✓
350	✓	✓	✓	✓
400	✓	✓	✓	✓

The heat-treatment was not applied to as synthesized carbon supported surfactant stabilized ruthenium nanoparticle catalyst, because it is well known that ruthenium itself is not an active species towards methanol electrooxidation reaction. However, cyclic voltammograms of carbon supported and unsupported ruthenium nanoparticle catalysts were taken to show their inactivity towards methanol electrooxidation and to indicate ruthenium's oxidation-reduction peaks on the electrode surface.

2.3. ELECTRODE PREPARATION FOR NANOPARTICLE CATALYSTS

The electrode solution was prepared by mixing 36,78 mg of prepared carbon supported powder catalyst, 0.5 ml of Nafion (Aldrich, 5 wt%), 0.15 ml of N,N-dimethyl formamide (Merck, 99.5%) and 2.5 ml of distilled water. The heterogeneous mixture was sonicated until almost homogenous dispersion of solid in solution was obtained. 50 µl of the slurry solution was dropped on the 0.7 cm diameter of glassy carbon which was used as a working electrode. Then, the electrode was dried at 40^{o}C for 20 minutes and settled on the glassy carbon at 100^{o}C for an hour (Gökağaç et al., 2001).

2.4. DETERMINATION OF METAL CONTENTS IN SYNTHESIZED NANOPARTICLE CATALYSTS

A certain amount of as synthesized carbon supported 1-hexanethiol stabilized Pt nanoparticle catalyst was heated at high temperature in a porcelain dish in order to remove carbon and unremoved surfactant content of catalyst, but metal. 100 ml of aqua regia [the mixture of 3 volumes of HCl (37%, Merck) and one volume of HNO_3 (65%, Merck)] was added to solid residue in order to dissolve metals. The mixture was then evaporated until the volume decreased to 25 ml and 25 ml of concentrated HCl was added to the solution. This process was repeated 4 times. Finally, the resulting solution was filtered and diluted to 100 ml with distilled water. The metal content of catalyst was determined by ICP-OES (Leeman Labs, Inc.).

2.5. PHYSICAL TECHNIQUES

2.5.1. CYCLIC VOLTAMMETRY

Linear sweep voltammetry (LSV) is a voltammetric technique in which the potential of a stationary electrode is changed linearly ("swept" or "scanned") toward increasingly negative or positive potentials until the electrode process of interest, either a reduction or oxidation, respectively, takes place. In practice, a variant on LSV is known as cyclic voltammetry, is much more commonly carried out. In cyclic voltammetry (CV), a normal LSV experiment is carried out, sweeping the potential from the initial potential E_1 to the final potential E_2, but the direction of voltage scan is reversed when E_2 is reached. Usually, the potential is swept back to E_1 on the second part of the voltammogram. This is done by applying a triangular voltage wave form (Figure 2.1.) to the electrode. Either one cycle (from E_1 to E_2 and back to E_1) or more than one cycle can be carried out. Scan rates can be varied (Figure 2.2.) over a wide range, thus, this is an extremely useful feature of CV.

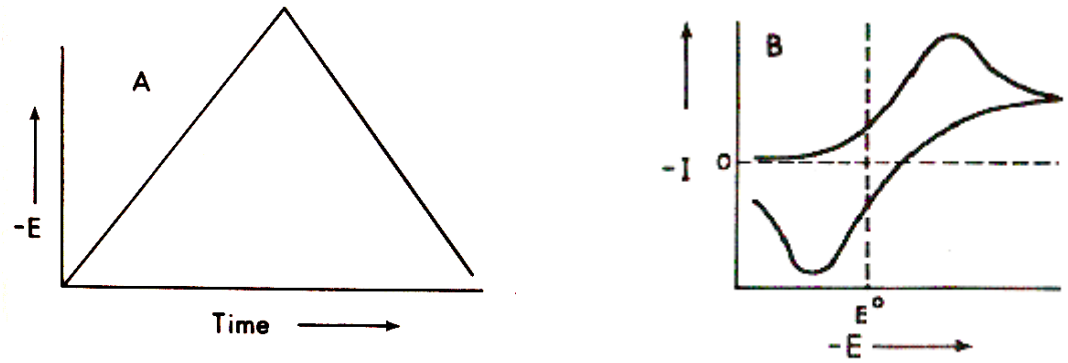

Figure 2.1. (A) Excitation signal; (B) Response is obtained for a single, simple reversible reduction when the voltage-time excitation signal extends considerably on both sides of the E^o for the reversible process.

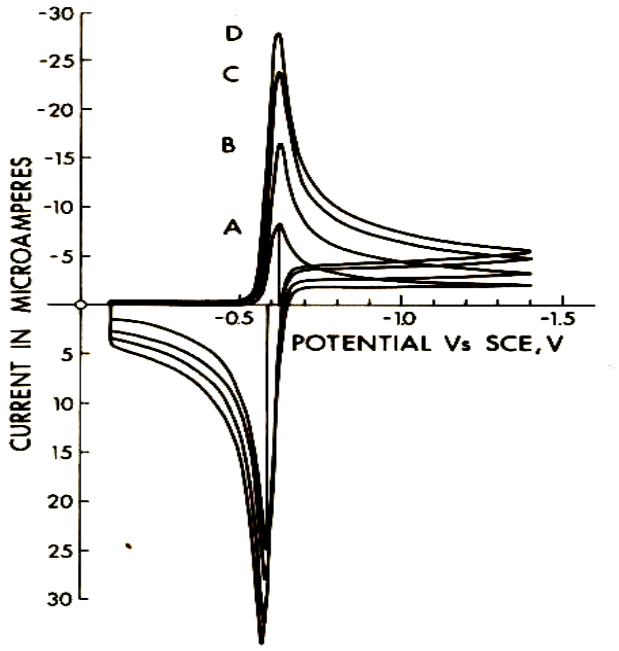

Figure 2.2. Cyclic voltammetry of a reversible process. Curve A, 20 mV/s; curve B, 50 mV/s; curve C, 100 mV/s; curve D, 200 mV/s. Initial scan is cathodic.

The measured parameters in cyclic voltammetry are the cathodic and anodic peak potentials, $E_{p,c}$ and $E_{p,a}$; the cathodic and anodic peak currents, $I_{p,c}$ and $I_{p,a}$; and the half peak potentials; which are the potentials $E_{p/2,c}$ and $E_{p/2,a}$ at which the cathodic and anodic currents reach half of their peak values. The independent variables are the voltage scan rate and the range of potential over which the scan is made. The former is the most important parameter in a diagnostic sense, although proper selection of scan range often can eliminate interference from other processes.

In a reversible system, the difference between the cathodic and anodic peak potentials, is equal to 0.059/n, where n is the number of electrons involved in the redox reaction; but in a quasi-reversible system, ΔE value is greater than this value. In an irreversible system, there is only one peak, no return wave. Figure 2.3. shows the cyclic voltammograms of a variety of reversible and irreversible systems, illustrating the

separation of the cathodic and anodic peaks as a function of the reversibility of the system.

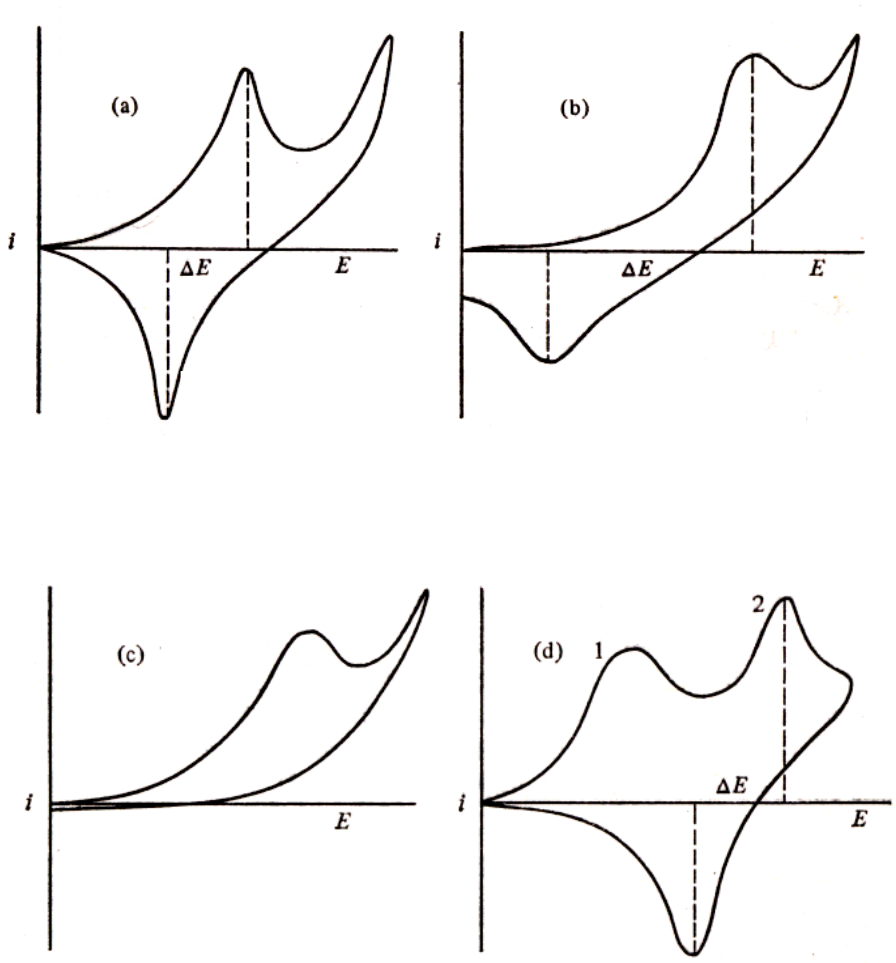

Figure 2.3. Cyclic voltammograms of a variety of reversible and irreversible systems.(a) Reversible process, ΔE=0.059/n, symmetrical; (b) Quasi-reversible process, ΔE>0.059/n, unequal peaks; (c) Single peak, no return wave; (d) Two species: 1 is irreversible, 2 is reversible.

The shape of cyclic voltammogram is highly dependent on the relative rates of electron transfer, mass transport (CV is carried out in quiet solution, hence diffusion is the only mode of mass transport) and any chemical reactions taking place at the electrode surface.

2.5.1.1. ELECTROCHEMICAL CELL DESIGN

The cyclic voltammetry measurements were performed with a conventional three electrode anodic cell (Figure 2.4) using Bank Wenking PGS 95 potentiostat/galvanostat (in Chemistry Department at METU) The working electrode was made up of catalysts settled on a 0.7 cm diameter glassy carbon. Saturated calomel electrode (SCE) and glassy carbon were used as the reference and counter electrodes, respectively. 0.1 M $HClO_4$ (60%, Merck) or 0.1 M $HClO_4$ + 0.4 M CH_3OH (99.8%, Merck) solutions were used as an electrolyte. Pure Ar gas was purged through electrolyte for at least 15 minutes prior to each experiment in order to remove oxygen in the electrolyte and electrochemical cell.

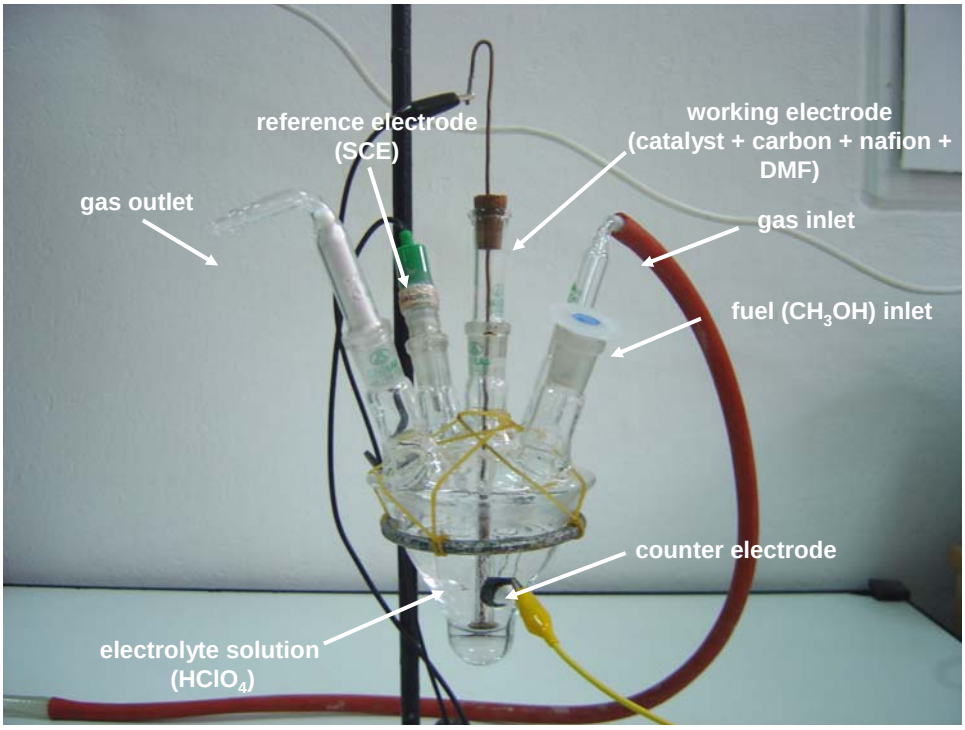

Figure 2.4. An electrochemical cell.

2.5.2. X-RAY DIFFRACTION

Diffraction of an X-ray beam striking a crystal occurs because the wavelength of the X-ray beam is similar to the spacing of atoms in minerals (1-10 Å). When an X-ray beam encounters the regular 3-D arrangement of atoms in a crystal, most of the X-rays will destructively interfere with each other and cancel each other out, but in some specific directions they constructively interfere and reinforce one another. These reinforced (diffracted) X-rays that produce the characteristic X-ray diffraction patterns are used for material identification.

W.L. Bragg (early 1900's) showed that diffracted X-rays act as if they were "reflected" from a family of planes within crystals. Bragg's planes are the rows of atoms that make up the crystal structure. These "reflections" were shown to only occur under certain conditions which satisfy the equation:

$n\lambda = 2d\sin\theta$ (Bragg Equation)

where n is an integer (1, 2, 3, ..., n); λ is the wavelength; d is the distance between atomic planes; and θ is the angle of incidence of the X-ray beam and the atomic planes. 2dsinθ is the path length difference between two incident X-ray beams where one X-ray beam takes a longer (but parallel) path because it "reflects" off an adjacent atomic plane. This path length difference must equal an integer value of the λ of the incident X-ray beams for constructive interference to occur such that a reinforced diffracted beam is produced.

For a given wavelength of incident X-rays and interplanar spacing (d) in a mineral, only specific θ angles will satisfy the Bragg equation. Example: focus a monochromatic X-ray beam (X-rays with a single wavelength) on a cleavage fragment of calcite and slowly rotate crystal. No "reflections" will occur until the incident beam makes an angle θ that satisfies the Bragg equation with n = 1. Continued rotation leads to other "reflections" at higher values of θ and correspond to when n = 2, 3, ... etc.; these known as 1st, 2nd, 3rd order, etc., "reflections".

Photographic plates were traditionally used to record the intensity and position of diffracted X-rays. Modern systems use diffractometers which are electronic X-ray counters (detectors) that can measure intensities much more accurately. Computers are used to process data and make necessary complex calculations. There are two main techniques:

(i) Single-Crystal Method: (X-ray beam is focused on a single crystal). Primary application is to determine atomic structure (symmetry, unit cell dimensions, space group, etc.,). Older methods (Laue method) used a stationary crystal with "white X-ray" beam (X-rays of variable wavelength) such that Bragg's equation would be satisfied by numerous atomic planes. The diffracted X-rays exiting the crystal all have different θ and thus produce "spots" on a photographic plate. The diffraction spots show the symmetry of the crystal. Modern methods (rotation, Weissenberg, precession, 4-circle) utilize various combination of rotating-crystal and camera setup to overcome limitations of the stationary methods (mainly the number of diffractions observed). These methods use monochromatic X-rays, but vary θ by moving the crystal mounted on a rotating stage. Usually employ diffractometers and computers for data collection and processing.

(ii) Powder Method: (X-ray beam focused on a powder pellet or powder smeared on a glass slide). This technique is essential for minerals that do not form large crystals (i.e. clays) and eliminates the problem of precise orientation necessary in single-crystal methods. Primary application is for mineral identification. Also can be used to determine mineral compositions (if d-spacing is a function of mineral chemistry) and to determine relative proportions of minerals in a mixture. Monochromatic X-rays are focused on pellet or slide mounted on rotating stage. Since sample is powder, all possible diffractions are recorded simultaneously from hypothetical randomly oriented grains. Mount is then rotated to ensure all diffractions are obtained. Older methods used photographic techniques. Most modern applications employ X-Ray Powder Diffractometers.

X-Ray powder diffractometry uses monochromatic X-rays on powder mounted on glass slide that is attached to a stage which systematically rotates into the path of the X-ray beam through $\theta = 0$ to 90°. The diffracted X-rays are detected electronically and recorded on an inked strip chart. The detector rotates simultaneously with the stage, but rotates through angles = 2θ. The strip chart also moves simultaneously with the stage and detector at a constant speed. The strip chart records the intensity of X-rays as the detector rotates through 2θ. Thus, the angle 2θ at which diffractions occur and the relative intensities can be read directly from the position and heights of the peaks on the strip chart. The Bragg equation is used to solve for the interplanar spacings (d) for all the major peaks and look up a match with JCPDS cards. JCPDS = Joint Committee on Powder Diffraction Standards.

In this work, synthesized nanoparticle catalyst particle sizes were calculated from X-ray diffraction pattern using line broadening of the peaks according to the Scherrer formula (Kinoshita and Stoneheart, 1977);

$$L = k\lambda / (\beta_{1/2} \text{Cos}\theta)$$

where $\beta_{1/2}$ is the breadth of a diffraction peak at half-height, measured in radians, λ is the wavelength of the incident X-rays, L is the effective crystallite diameter, θ is the position of the peak maximum and k is a constant [taken to be 0.9 as recommended by Klug and Alexander (1962)]. X-ray powder diffraction (XRD) patterns were taken by using Rigaku diffractometer with Ultima + theta-theta high resolution goniometer

and Cu (Kα, 40 kV, 40 mA, λ = 1.54056Å) radiation in Metallurgy Engineering Department at METU.

2.5.3. TRANSMISSION ELECTRON MICROSCOPY

The transmission electron microscope (TEM) has become the premier tool for the microstructural characterization of materials. In practice, the diffraction patterns measured by X-ray methods are more quantitative than electron diffraction patterns, but electrons have an important advantage over X-ray, they can be focused easily. The optics of electron microscope can be used to make images of the electron intensity emerging from the sample. For example, variations in the intensity of electron diffractions across a thin specimen, called "diffraction contrast", is useful for making images of defects such as dislocations, interfaces, and second phase particles. Beyond diffraction contrast microscopy, which measures the intensity of diffracted waves, in "high resolution" transmission emission microscopy (HRTEM or HREM) the phase of the diffracted electron wave is preserved and interferes constructively or destructively with the phase of transmitted wave. This technique of "phase-contrast imaging" is used to form images of columns of atoms. TEM is such a powerful tool for the characterization of materials that some microstructural features are defined largely in terms of their TEM images.

Besides diffraction and spatial imaging, the high-energy electrons in TEM cause electronic excitations of the atoms in the specimen. "Analytical TEM" uses two types of spectrometries to obtain chemical information from electronic excitations:

(a) In energy-dispersive X-ray spectrometry (EDS), an X-ray spectrum is acquired from small regions of the specimen illuminated with a focused electron beam, usually using a solid-state detector. Characteristic X-rays from the chemical elements are used to determine the concentrations of the different elements in the specimen.

(b) In electron energy-loss spectrometry (EELS), energy losses of the electrons are measured after the high-energy electrons have traversed the specimen.

(c) Information on local chemistry and structure is obtained from features in EELS spectra caused by plasmon excitations and core electron excitations.

A block diagram of a TEM is shown in Figure 2.5. A modern TEM may have the capability of imaging the variations in diffraction across the specimen (diffraction contrast imaging), imaging the phase contrast of the specimen (high-resolution imaging), obtaining diffraction patterns from selected areas of the specimen, and performing EELS and EDS spectroscopy measurements with a small, focused electron beam.

In this study, transmission emission micrographs of carbon supported heat-treated nanoparticle catalysts were taken by Jeol JEM 3010, 300 kV (at Kırıkkale University) and Leo 906-E, 120 kV (at Ankara University - İbni Sina Hospital). Sample preparation for TEM involved dispersion of the carbon supported material in carbon tetrachloride using an ultrasonic bath. This solution was then dropped onto a 400 mesh copper grid and left to dry at room temperature.

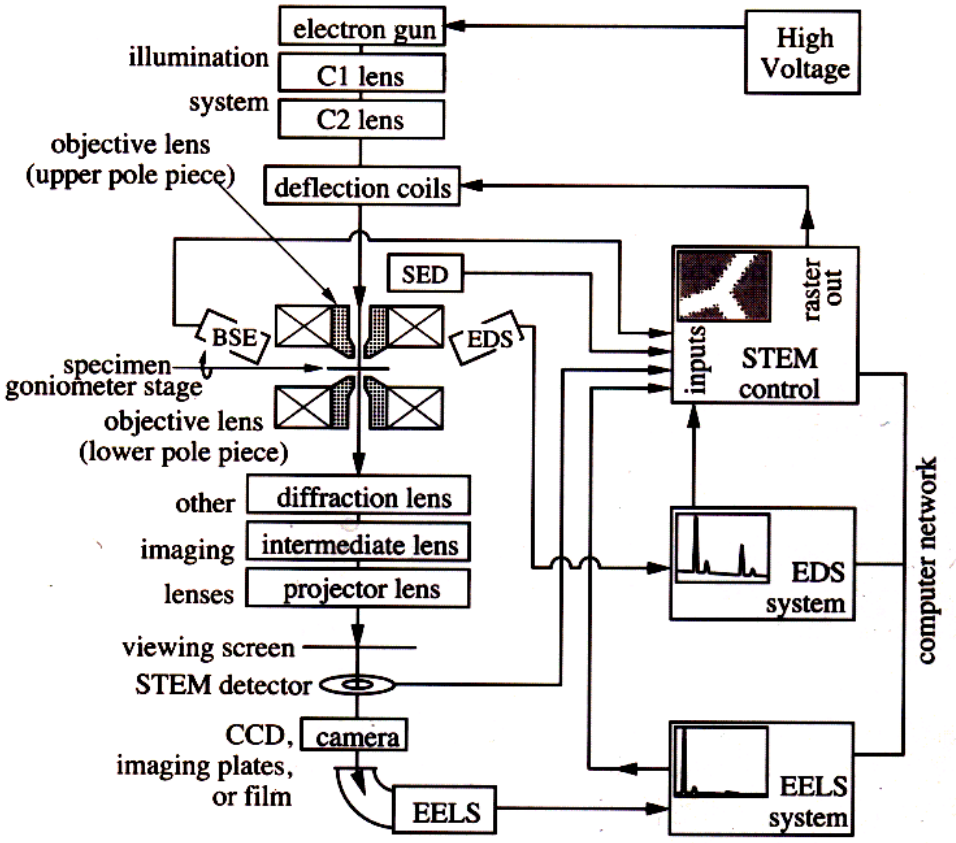

Figure 2.5. Block diagram of typical TEM with STEM (Scanning Transmission Electron Microscopy) capability.

2.5.4. X-RAY PHOTOELECTRON SPECTROSCOPY

Photoelectron spectroscopy differs from the other spectroscopic techniques in which the characteristics of absorbed, emitted, or scattered electromagnetic radiation are measured; instead the kinetic energies of ionized electrons are monitored, because the collision of photons with atoms or molecules can result in the ejection of photoelectrons.

X-ray photoelectron spectroscopy (called variously XPS or ESCA - Electron Spectroscopy for Chemical Analysis), employing X-ray radiation as the ionizing source, has been largely concerned with the ejection of core electrons as shown in Figure 2.6.

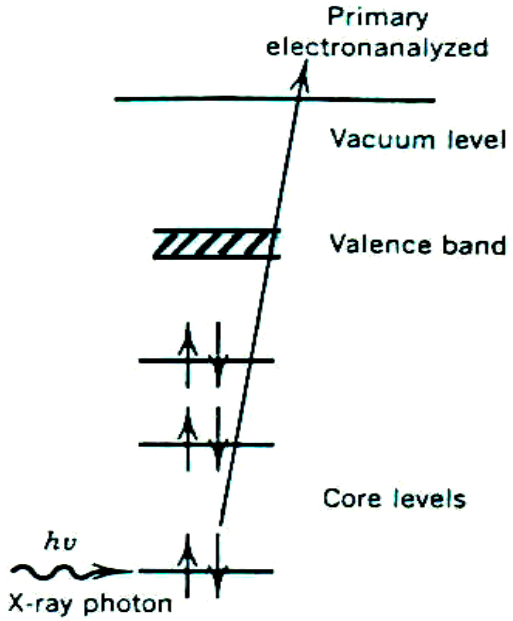

Figure 2.6. The energies of electrons ejected from core levels in X-ray photoelectron spectroscopy (XPS).

The energy, required to liberate an electron from a system, using the vacuum as a reference level, E_b, can be calculated from a consideration of energy conversation:

$$E_b = E_{source} - E_{kin} - E_r$$

where E_{source} is the energy of the ionizing radiation, E_{kin} is the kinetic energy of the photoelectron, and E_r is the recoil energy of the atom or molecule. A photoelectron spectrum is thus a plot of the number of photoelectrons incident upon a suitable counting device as a function of the kinetic energy of the photoelectrons.

The usual sources of X-rays are Mg Kα (1253.6 eV) or Al Kα (1486.6 eV). Since the energies of atomic core levels are characteristic of each element, XPS can be used to obtain an elemental analysis of the surface. This type of spectroscopy is referred as ESCA (Electron Spectroscopy for Chemical Analysis) or EDS (Energy Dispersive X-Ray Spectroscopy). The relative amounts of elements in sample can be determined by these methods. The ionization potential of atomic core level depends

to some extend on the chemical environment of the atom, so that information can also be obtained around the type of bonding between adsorbate and the surface and oxidation state of each element.

In this study, the binding energies of Pt $4f_{7/2}$ and $4f_{5/2}$, Ru $3d_{5/2}$ and $3d_{3/2}$, S $2p_{3/2}$ and $2p_{1/2}$ and C1s electrons were determined for synthesized Pt, Ru, $Pt_{75}Ru_{25}$ and $Pt_{97}Ru_3$ nanoparticle catalysts by Specs spectrometer using Kα lines of Mg (1253.6 eV, 10 mA) as a X-ray source at Central Labortory of METU. The spectrometer has two stainless steel chambers with independent pumping systems. The first chamber is a fast entry lock working between 10^{-4}-10^{-5} torr. The second chamber operates between 10^{-9}-10^{-10} torr and is used to remove high volatile gases. The second chamber is the main chamber where the spectroscopic values are taken by a hemispherical analyser with a multichannel detector. The Ar^+ ion flood was used to clean the surface when necessary. Samples were held in a copper holder with double-sided tape. All lines were referenced to the C 1s line at 284.6 eV. Peak fittings of Pt $4f_{7/2}$ - $4f_{5/2}$, Ru $3d_{5/2}$ - $3d_{3/2}$ and S $2p_{3/2}$ - $2p_{1/2}$ regions of nanoparticle catalysts were done using Origin_Pro_7_Microcal peak fit programme.

CHAPTER III

RESULTS AND DISCUSSION

3.1. CYCLIC VOLTAMMETRY

3.1.1. CYCLIC VOLTAMMOGRAMS OF CARBON SUPPORTED 1-HEXANETHIOL STABILIZED PLATINUM NANOPARTICLE CATALYST WITH 1:1 THIOL/PLATINUM MOLAR RATIO

Cyclic voltammograms of all heat-treated carbon supported 1-hexanethiol stabilized platinum nanoparticle catalysts were recorded in 0.1 M $HClO_4$ at room temperature with a scan rate of 50 mV/s. Although small shifts in the position of the some of the peaks were observed, the cyclic voltammograms of all samples were similar and a typical example was shown in Figure 3.1. The hydrogen adsorption region of cyclic voltammograms in anodic current was observed with a broad and intense peak at ~ -150 mV. The rapid decrease in cathodic current below ~ -300 mV was detected due to the bulk hydrogen evolution. Although it was difficult to differentiate the regions from each other, it was generally believed that the adsorption of H_2O on Pt appeared above ~ 650 mV and the formation of bulk platinum oxide and oxygen evolution were observed at potential above ~ 1000 mV (Equations 3.1., 3.2., 3.3.). Platinum oxide and carbon hydroquinone reductions started at ~ 500 mV and attained maxima at ~ 350 mV on the cathodic sweep.

$$Pt + H_2O \rightarrow Pt–OH_{(ads)} + H^+ + e^- \quad (3.1.)$$

$$Pt–OH_{(ads)} \rightarrow Pt–O_{(ads)} + H^+ + e^- \quad (3.2.)$$

$$Pt–O_{(ads)} \rightarrow PtO \quad (3.3.)$$

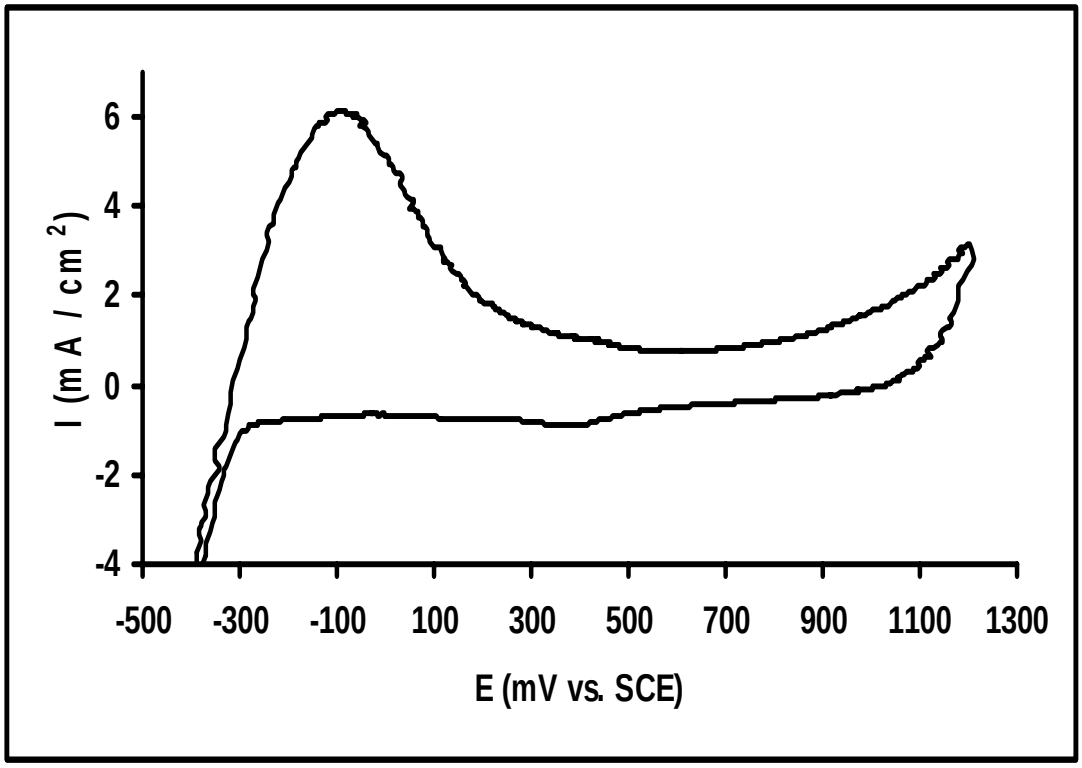

Figure 3.1. Cyclic voltammogram of thiol stabilized Pt/C nanoparticle catalyst (1:1 thiol/Pt molar ratio, heated up at 200°C for 5 hours) in 0.1 M $HClO_4$ at room temperature. Scan rate is 50 mV/s.

The addition of methanol to the $HClO_4$ electrolyte resulted in a dramatic change in the appearance of the voltammogram, Figure 3.2. Methanol oxidation reaction started at ~ 350 mV and reached maxima at ~ 750 mV in anodic sweep. Above ~ 800 mV methanol oxidation reaction was inhibited and anodic current decreased until the potential, where the oxygen evolution region onset. On the reverse scan, platinum oxide reduction was observed before methanol oxidation reaction recommenced at ~ 700 mV.

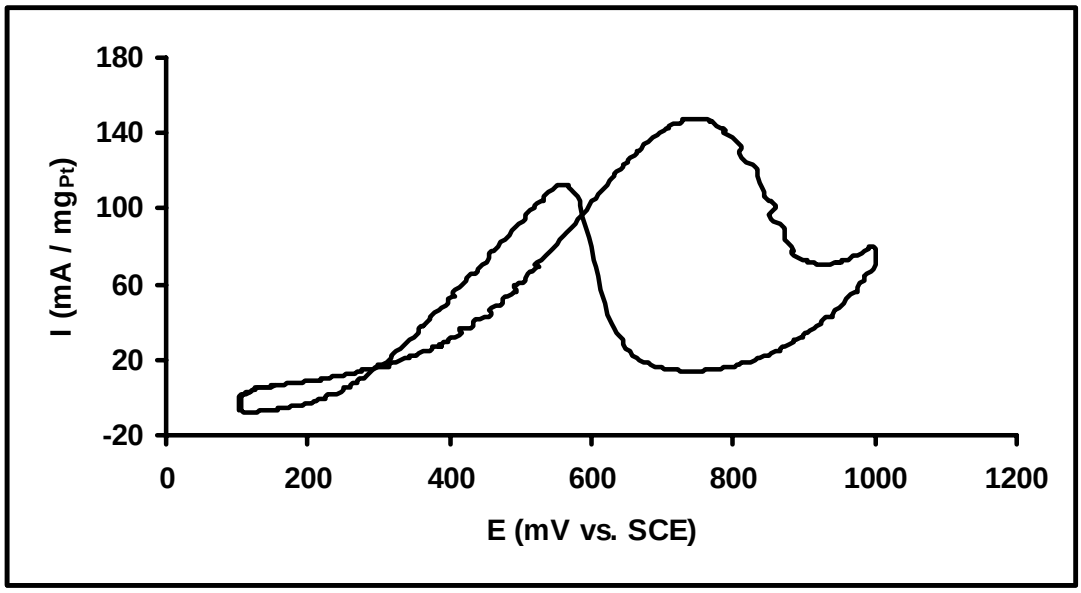

Figure 3.2. Cyclic voltammogram of thiol stabilized Pt/C nanoparticle catalyst (1:1 thiol/Pt molar ratio, heated up at 200^{o}C for 5 hours) in 0.1 M $HClO_4$ + 0.4 M CH_3OH at room temperature. Scan rate is 50 mV/s.

It is well known that prepared platinum nanoparticles containing catalysts were covered by 1-hexanethiol surfactants inherently. Therefore, it was not possible to use as prepared platinum nanoparticle catalyst for methanol oxidation reaction. In order to hopefully remove the surfactants and to observe the effect of temperature on carbon supported catalyst, the catalyst was heated up at 100^{o}C, 150^{o}C, 200^{o}C, 250 ^{o}C, 300^{o}C, 350^{o}C and 400^{o}C for 2, 5, 10 and 20 hours, Table 3.1.

Only the anodic region of the cyclic voltammograms were given in order to represent the methanol oxidation reaction clearly, Figure 3.3., 3.4., 3.5., 3.6. The maximum activity towards methanol oxidation reaction was observed for the catalysts which were heated up at 200^{o}C for different time intervals. After 200^{o}C, the activity of catalyst towards methanol oxidation reaction decreased. This might be due to agglomeration of platinum nanoparticles.

Table 3.1. Heat-treatment experiments for 1-hexanethiol stabilized Pt/C nanoparticle catalyst.

Time (h) / Temp. (°C)	2	5	10	20
100	✓	✓	✓	✓
150	✓	✓	✓	✓
200	✓	✓	✓	✓
250	✓	✓	✓	✓
300	✓	✓	✓	✓
350	✓	✓	✓	✓
400	✓	✓	✓	✓

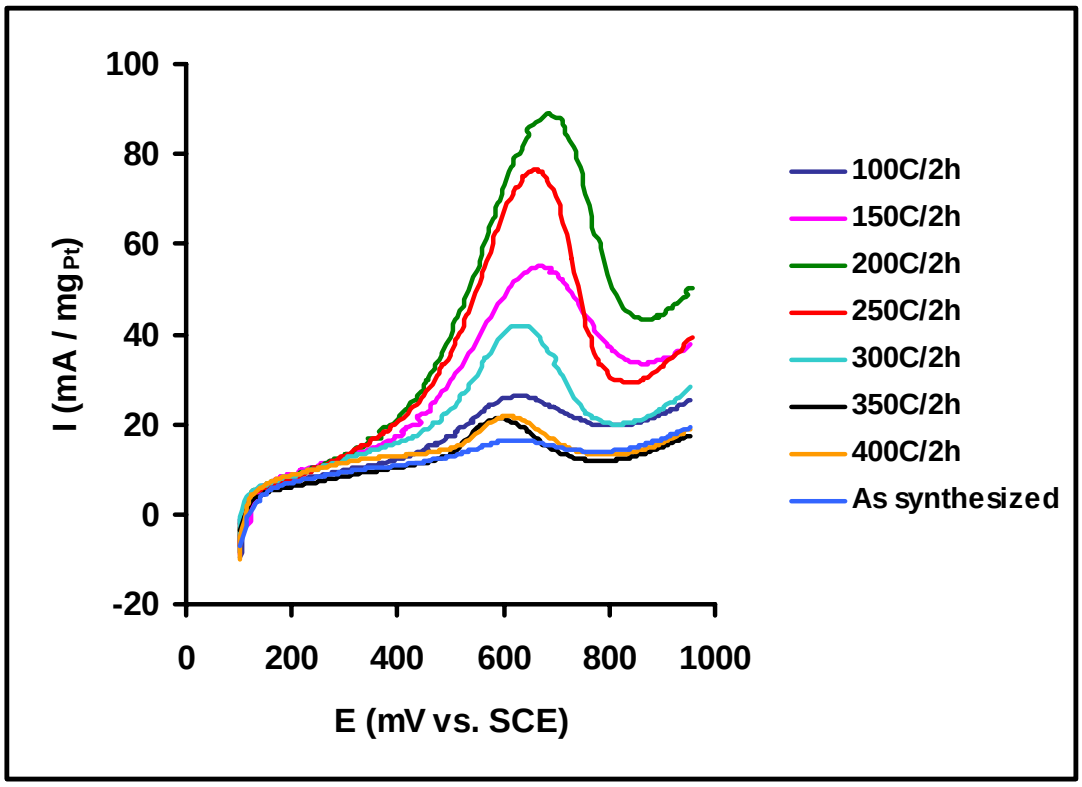

Figure 3.3. Cyclic voltammograms of thiol stabilized Pt/C nanoparticle catalyst (1:1 thiol/Pt molar ratio, heated up for 2 hours between 100-400 °C) in 0.1 M $HClO_4$ + 0.4 M CH_3OH at room temperature. Scan rate is 50 mV/s.

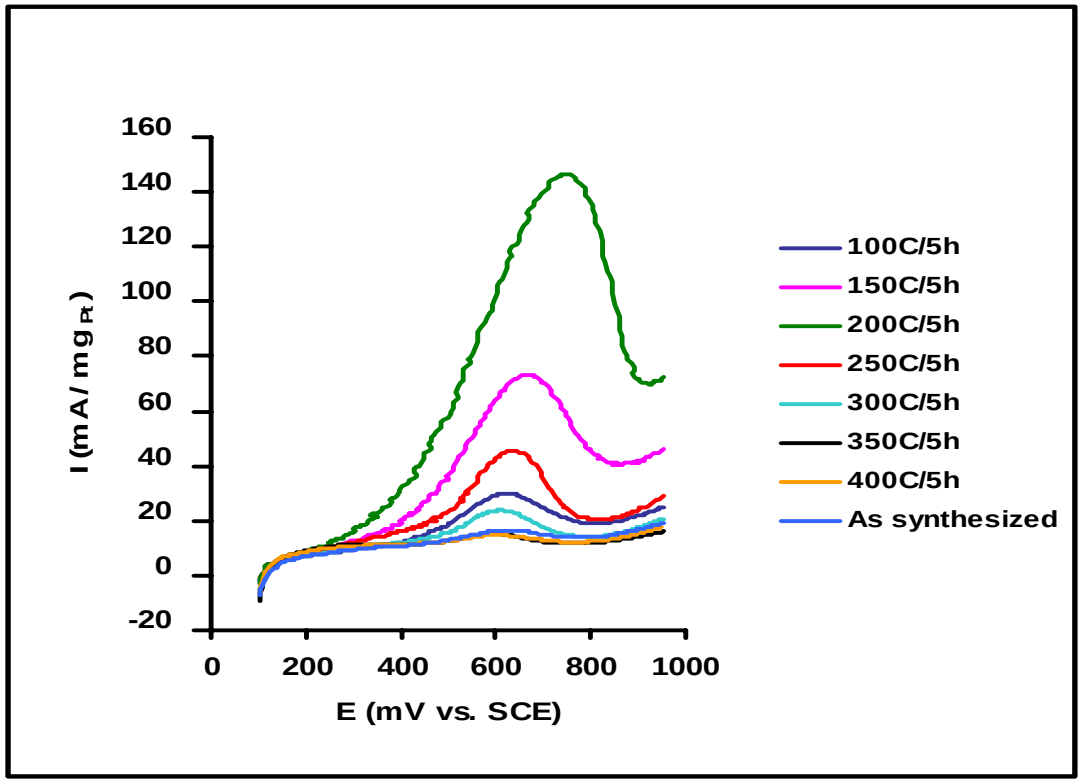

Figure 3.4. Cyclic voltammograms of thiol stabilized Pt/C nanoparticle catalyst (1:1 thiol/Pt molar ratio, heated up for 5 hours between 100-400 ^{o}C) in 0.1 M $HClO_4$ + 0.4 M CH_3OH at room temperature. Scan rate is 50 mV/s.

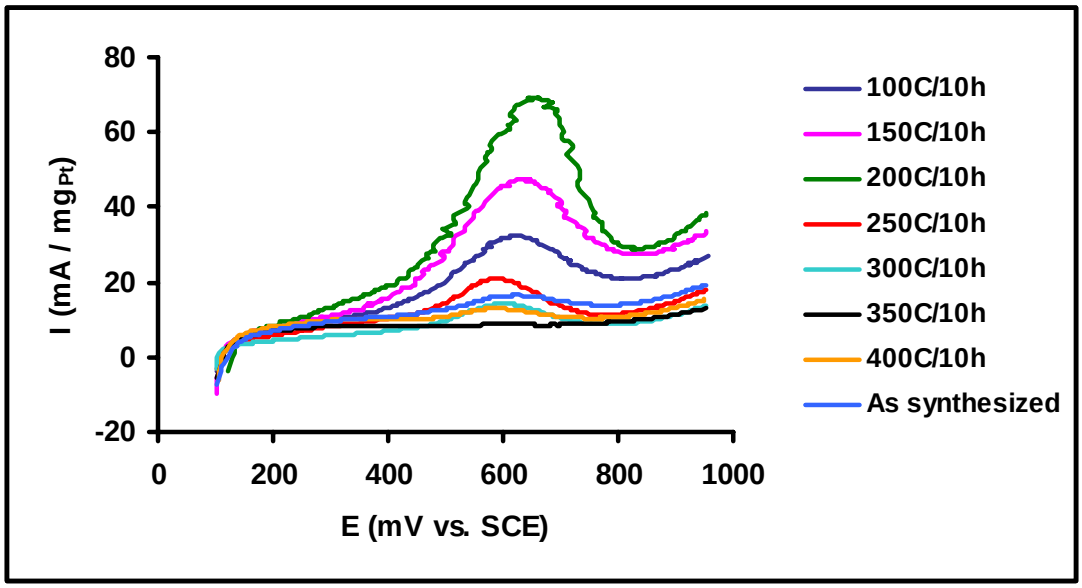

Figure 3.5. Cyclic voltammograms of thiol stabilized Pt/C nanoparticle catalyst (1:1 thiol/Pt molar ratio, heated up for 10 hours between 100-400 ^{o}C) in 0.1 M $HClO_4$ + 0.4 M CH_3OH at room temperature. Scan rate is 50 mV/s.

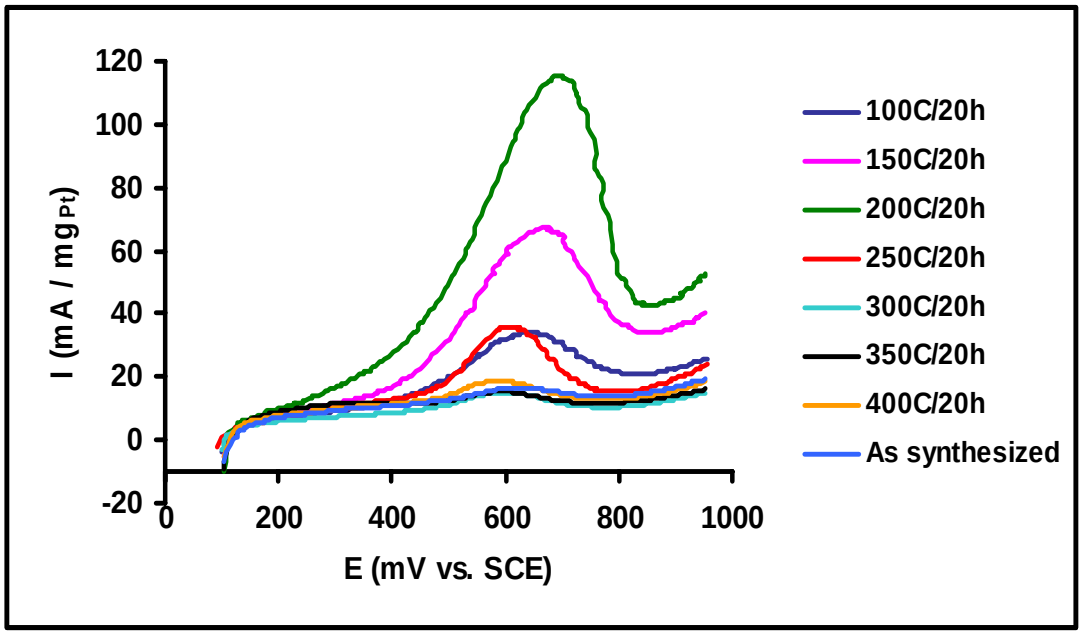

Figure 3.6. Cyclic voltammograms of thiol stabilized Pt/C nanoparticle catalyst (1:1 thiol/Pt molar ratio, heated up for 20 hours between 100-400 ^{o}C) in 0.1 M $HClO_4$ + 0.4 M CH_3OH at room temperature. Scan rate is 50 mV/s.

The catalysts, which have the highest methanol oxidation reaction capacity for each set of time interval, were considered together and the maximum activity was observed for the catalyst which was heated up at 200^{o}C for 5 hours, Figure 3.7. This might be due to observation of optimum platinum nanoparticle size distribution on carbon support and oxidation states, which will be given in TEM and XPS sections, respectively.

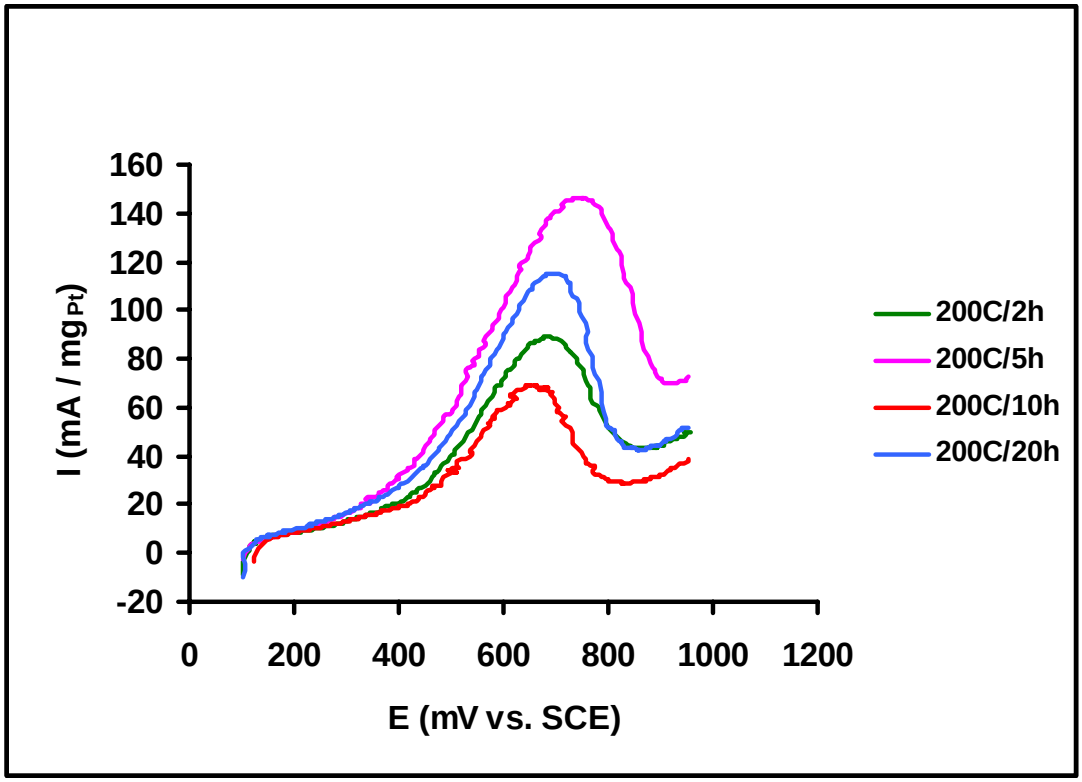

Figure 3.7. Cyclic voltammograms of the most active thiol stabilized Pt/C nanoparticle catalysts (1:1 thiol/Pt molar ratio) for each heating time interval in 0.1 M $HClO_4$ + 0.4 M CH_3OH at room temperature. Scan rate is 50 mV/s.

3.1.2. CYCLIC VOLTAMMOGRAMS OF CARBON SUPPORTED AND UNSUPPORTED 1-HEXANETHIOL STABILIZED RUTHENIUM NANOPARTICLE CATALYSTS WITH 1:1 THIOL/RUTHENIUM MOLAR RATIO

In order to characterize the surface of ruthenium nanoparticles, the cyclic voltammogram of carbon unsupported ruthenium nanoparticle catalyst was recorded in 0.1 M $HClO_4$ at room temperature with a scan rate of 50 mV/s, Figure 3.8. As described by Goodenough and co-workers (Goodenough et al., 1990), the voltammogram of a freshly prepared electrode showed two redox features which were ascribed to oxidation of the surface of Ru(II) to Ru(III) at ~ -100 mV and

Ru(III) to Ru(IV) at ~ 600 mV couples on anodic sweep. Their reduction features were noticed at -200 and +150 mV, respectively, on cathodic sweep.

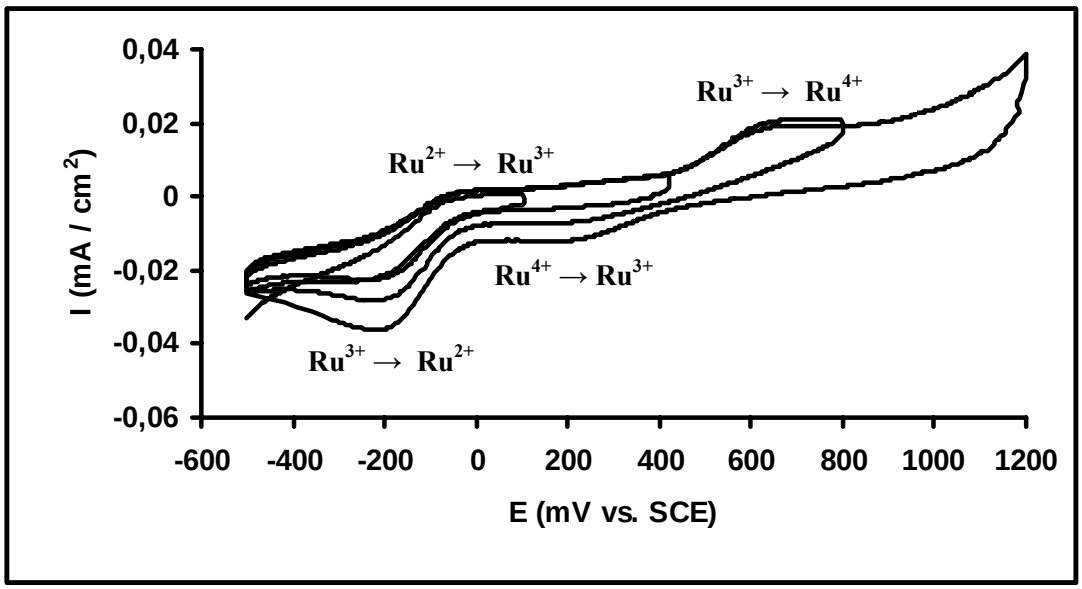

Figure 3.8. Cyclic voltammogram of carbon unsupported as synthesized thiol stabilized ruthenium nanoparticle catalyst (1:1 thiol/ruthenium molar ratio) in 0.1 M $HClO_4$. Scan rate is 50 mV/s.

It was well known that ruthenium nanoparticles were covered with 1-hexanethiol stabilizer during the preparation process and it was very difficult to remove this shell around the ruthenium nanoparticles. To define the electrochemical behaviour of 1-hexanethiol in carbon and in prepared Ru/C nanoparticle catalyst, cyclic voltammograms of 1-hexanethiol/C, Ru/C nanoparticle catalyst and carbon support itself were recorded in 0.1 M $HClO_4$ at room temperature with a scan rate of 50 mV/s, Figure 3.9. While cyclic voltammograms of carbon support itself showed oxidation-reduction couple of hydroquinone between ~ 0 and 400 mV (Bard et al., 1985), 1-hexanethiol on carbon revealed some oxidation-reduction features between -200 and +500 mV, which was difficult to interpret, and an intense broad peak at ~ 1000 mV. This feature was ascribed for the formation of 1-hexanethiol dimer, HT_2,

Equation 3.4., as was noticed dimer formation of xanthates such as potassium ethyl xanthate, KEX, Equation 3.5. (Grano et al., 1997).

$$2\ C_6H_{13} - S - H \rightarrow C_6H_{13} - S - S - C_6H_{13} + 2\ H^+ + 2\ e^- \qquad (3.4.)$$

$$2\ C_2H_5 - O - \overset{\overset{S}{\|}}{C} - S^-K^+ \rightarrow C_2H_5 - O - \overset{\overset{S}{\|}}{C} - S - S - \overset{\overset{S}{\|}}{C} - O - C_2H_5 + 2\ K^+ + 2\ e^- \qquad (3.5.)$$

Cyclic voltammogram of carbon supported 1-hexanethiol stabilized Ru nanoparticle catalyst exhibited an intense shifted broad feature for HT_2, at ~ 900 mV in addition to the oxidation-reduction couple of hyroquinone.

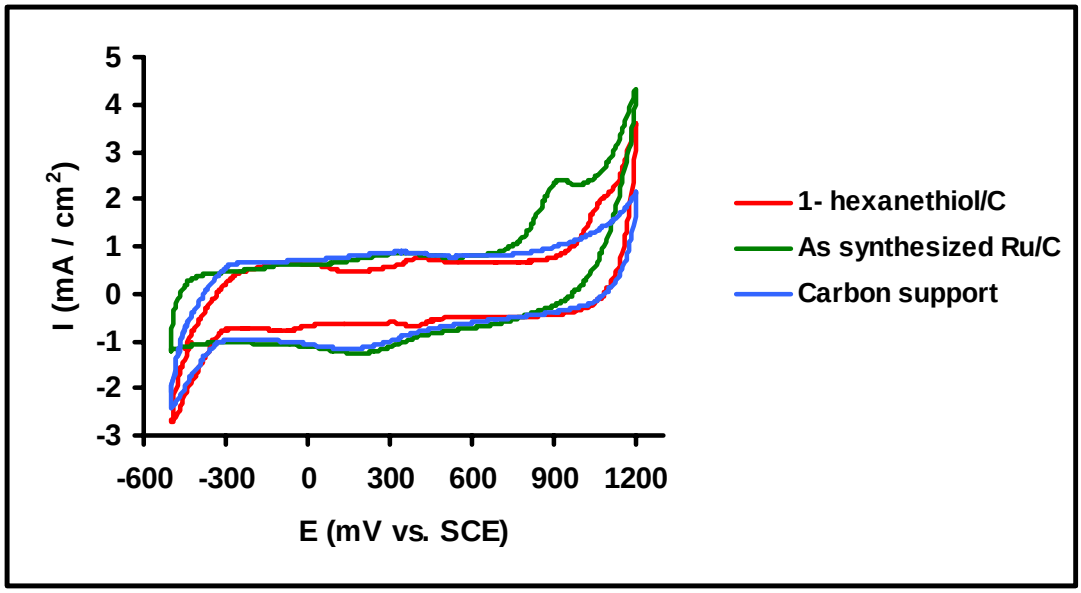

Figure 3.9. Cyclic voltammograms of 1-hexanethiol/C, as synthesized thiol stabilized Ru/C nanoparticle catalyst (1:1 thiol/ruthenium molar ratio) and carbon support itself in 0.1 M $HClO_4$ at room temperature. Scan rate is 50 mV/s.

The cyclic voltammograms of carbon unsupported thiol stabilized ruthenium nanoparticle catalyst was recorded in 0.1 M $HClO_4$ and in 0.1 M $HClO_4$ + 0.4 M CH_3OH, Figure 3.10. Both cyclic voltammograms were the same, methanol

oxidation reaction could not be achieved on ruthenium nanoparticles as expected but Ru(II)/Ru(III) couple and 1-hexanethiol dimerization features were clearly observed.

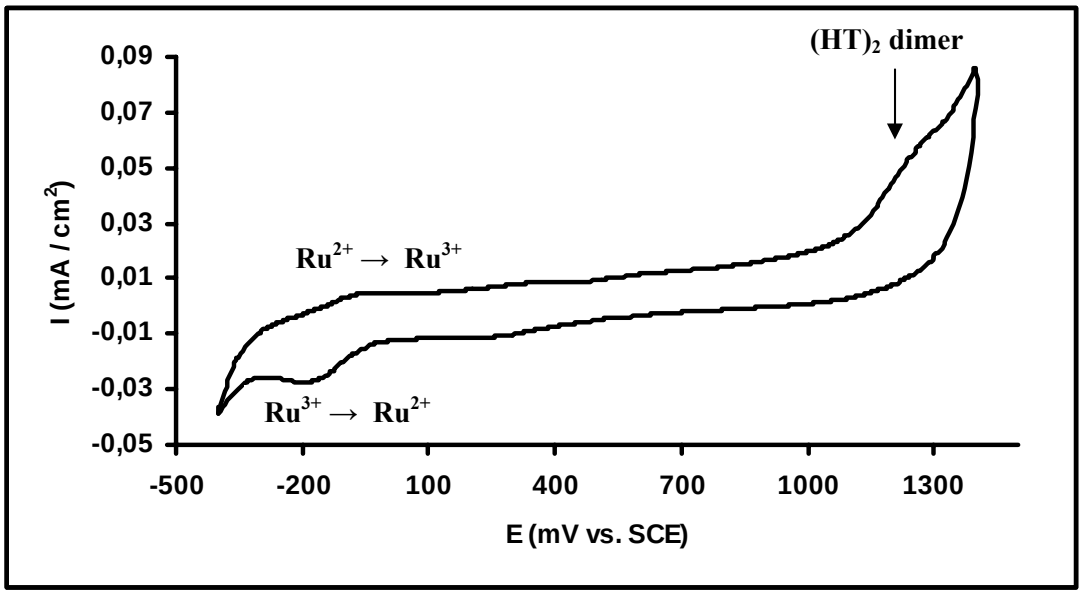

Figure 3.10. Cyclic voltammogram of carbon unsupported as synthesized thiol stabilized ruthenium nanoparticle catalyst (1:1 thiol/ruthenium molar ratio) in 0.1 $HClO_4$ + 0.4 M CH_3OH. Scan rate is 50 mV/s.

3.1.3. CYCLIC VOLTAMMOGRAMS OF CARBON SUPPORTED 1-HEXANETHIOL STABILIZED $Pt_{75}Ru_{25}$ AND $Pt_{97}Ru_3$ NANOPARTICLE CATALYSTS WITH 1:1 THIOL/PtRu MOLAR RATIO

In order to characterize the extent of interaction between Ru and Pt, cyclic voltammogram studies in 0.1 M $HClO_4$ at room temperature were undertaken. The cyclic voltammograms of $Pt_{75}Ru_{25}$/C and $Pt_{97}Ru_3$/C electrodes were very similar to that shown in Figure 3.11. It was possible to observe Pt, Ru and surfactant features on the cyclic voltammogram in addition to hydrogen oxidation (~ -200 mV), hydrogen reduction (~ -300 mV), oxygen evolution (>1000 mV) and reduction of platinum oxide (~ 350 mV) on the surface of platinum nanoparticles. Ruthenium

reduction couples Ru(IV)/Ru(III) and Ru(III)/Ru(II) were observed at ~ 150 mV and ~ -200 mV, respectively. The corresponding oxidation features were prohibited by intense hydrogen oxidation features. 1-hexanethiol dimer peak was also observed at ~ 900 mV on anodic sweep as described in the previous section. It should be stressed that the marked increase in the background current with scan was a result of an opening of the porous structure of the carbon electrode, which effectively increased the observed surface area, and was typically observed in all the electrodes studied.

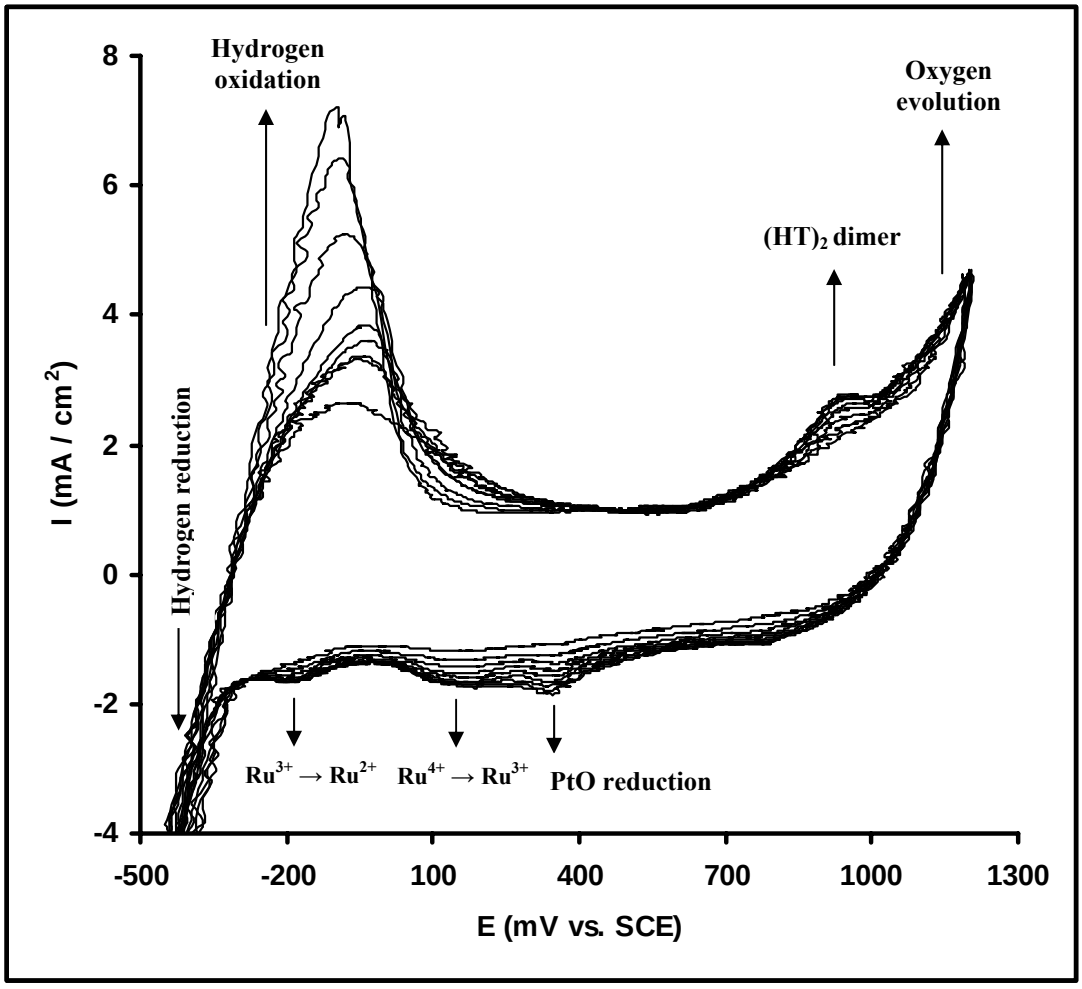

Figure 3.11. Cyclic voltammograms of thiol stabilized $Pt_{75}Ru_{25}$/C nanoparticle catalyst (1:1 thiol/PtRu molar ratio, heated up for 10 hours at 200°C) in 0.1 M $HClO_4$ at room temperature. Scan rate is 50 mV/s.

Addition of methanol to the $HClO_4$ electrolyte resulted change in the appearance of the voltammogram as shown in Figure 3.12. Examination of the cyclic voltammograms of $Pt_{75}Ru_{25}/C$ and $Pt_{97}Ru_3/C$ catalyst in 0.1 M $HClO_4$ + 0.4 M CH_3OH was indicated that methanol oxidation reaction started at ~ 300 mV, it was inhibited above 700 mV that cause decrease in anodic current until the oxygen evolution region. On the cathodic (reverse) scan, methanol oxidation reaction starts at ~ 500 mV after platinum oxide reduction. In addition to methanol oxidation reaction it was also possible to observe disappearance of features of Ru(IV)/Ru(III) and Ru(III)/Ru(II) couples with time.

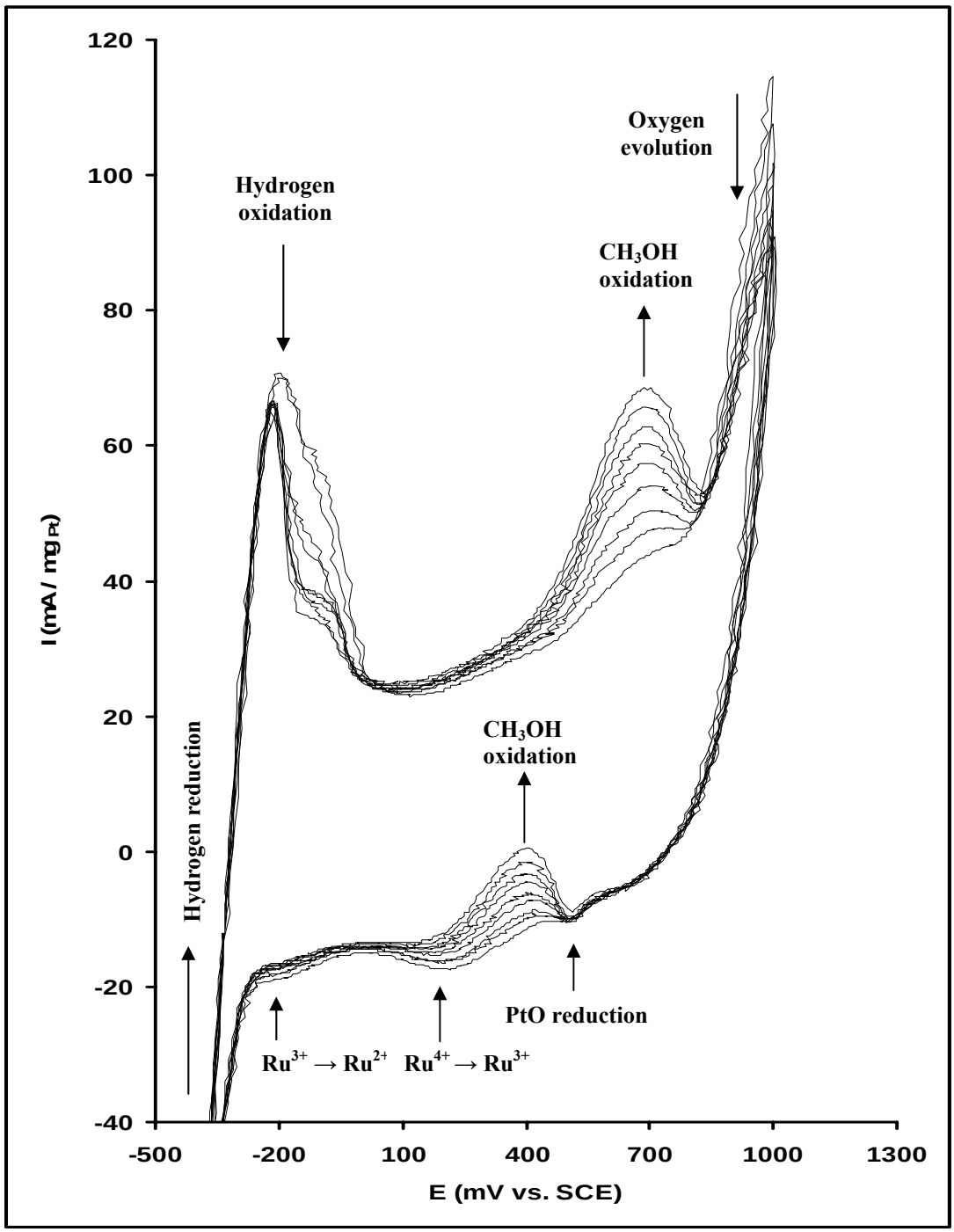

Figure 3.12. Cyclic voltammograms of thiol stabilized $Pt_{75}Ru_{25}$/C nanoparticle catalyst (1:1 thiol/PtRu molar ratio, heated up for 10 hours at 200°C) in 0.1 M $HClO_4$ + 0.4 M CH_3OH at room temperature. Scan rate is 50 mV/s.

In order to determine the effect of addition of second metal, which was Ru, in the catalyst, cyclic voltammogram of $Pt_{75}Ru_{25}$/C and $Pt_{97}Ru_3$/C were recorded in 0.1 M $HClO_4$ + 0.4 M CH_3OH at room temperature. Small activity towards methanol oxidation reaction was observed for both type of unheated prepared catalysts. The maximum activity observation after heating of 1-hexanethiol stabilized Pt/C catalyst at 200^oC was the reason to heat up $Pt_{75}Ru_{25}$/C and $Pt_{97}Ru_3$/C at 200^oC for different time interval. The maximum activities were observed for the $Pt_{75}Ru_{25}$/C and $Pt_{97}Ru_3$/C catalysts which were heated up at 200^oC for 20 hours as shown in Figure 3.13 and 3.14. The positive result towards methanol oxidation reaction was possible due to removing of 1-hexanethiol missile shell around the metal nanoparticles. However, their activities were still lower than the 1-hexanethiol stabilized Pt/C catalyst as shown in Figures 3.13. and 3.14. It was believed that this might be due to partially coverage of platinum nanoparticles by ruthenium metal or incomplete removing of 1-hexanethiol missile shell around the metal nanoparticles which decrease the active surface area of metal. In order to examine the latter reason, the $Pt_{75}Ru_{25}$/C and $Pt_{97}Ru_3$/C were heated up at high temperature such as 300^oC, 400^oC, 500^oC and 600^oC for 5 hours. Only anodic part of the cyclic voltammograms of those prepared catalysts were recorded in 0.1 M $HClO_4$ + 0.4 M CH_3OH at room temperature, Figure 3.15 and 3.16. Similar type of trend was observed for both catalysts except observation of extra peak for $Pt_{75}Ru_{25}$/C at ~ 400 mV might be due to surfactant or methanol oxidation reaction on Pt/Ru surface area. The catalysts which were heated up at 500^oC for 5 hours had the highest activities towards methanol oxidation reaction while the catalysts which were heated up at 600^oC for 5 hours were the least active ones. The highest activity observation at 500^oC might be due to removal of surfactants and formation of suitable composition on nanoparticles and agglomeration of appropriate nanoparticle size. Sudden decrease in the activity of catalysts which were heated up at 600^oC for 5 hours, towards methanol oxidation reaction might be due to formation of large agglomerated particles which caused to decrease the active surface area of metals. There was no direct relationship between heating temperature and the activity of the catalyst as in carbon supported 1-hexanethiol stabilized platinum nanoparticle catalyst. This result might tell us electrocatalytic activities were not a simple function of Pt/Ru and metal/surfactant ratios but appearently a number of factors such as particle size, crystallite

distribution, surface composition, oxidation state of metal, metal-metal and metal-support interactions were also important.

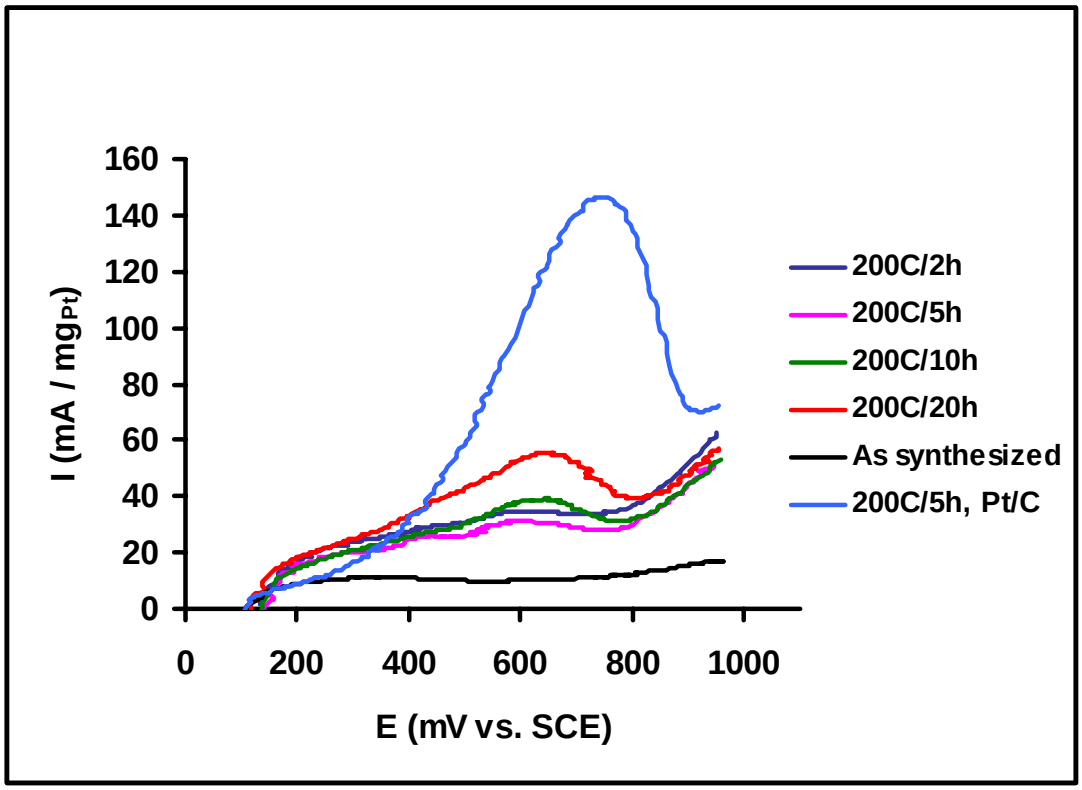

Figure 3.13. Cyclic voltammograms of thiol stabilized Pt/C and $Pt_{75}Ru_{25}$/C nanoparticle catalysts (1:1 thiol/PtRu molar ratio, heated up for different time interval at 200°C) in 0.1 M $HClO_4$ + 0.4 M CH_3OH at room temperature. Scan rate is 50 mV/s.

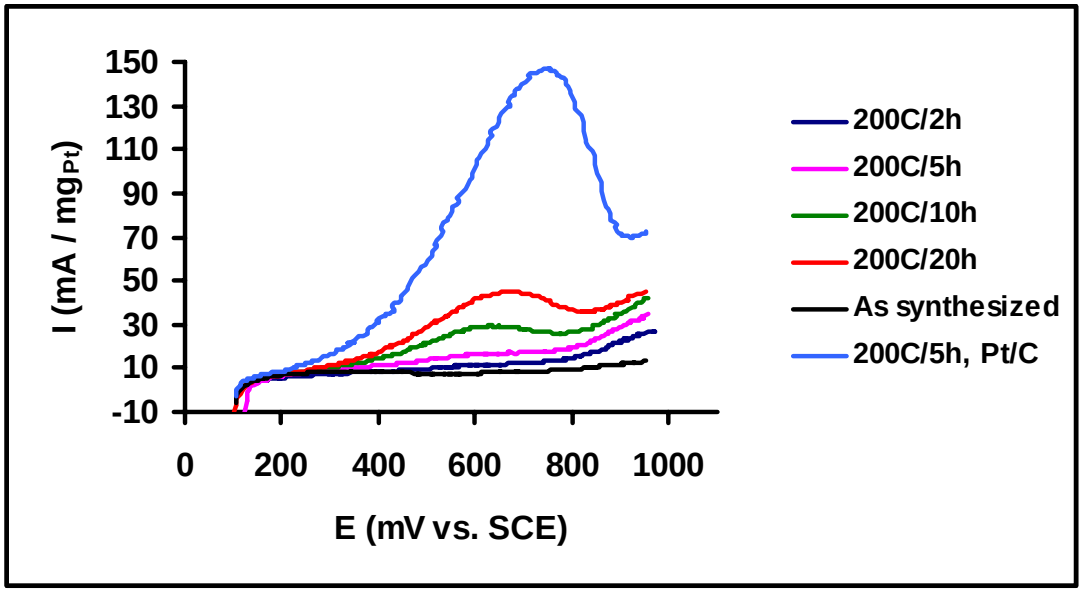

Figure 3.14. Cyclic voltammograms of thiol stabilized Pt/C and $Pt_{97}Ru_3$/C nanoparticle catalysts (1:1 thiol/PtRu molar ratio, heated up for different time interval at 200°C) in 0.1 M $HClO_4$ + 0.4 M CH_3OH at room temperature. Scan rate is 50 mV/s.

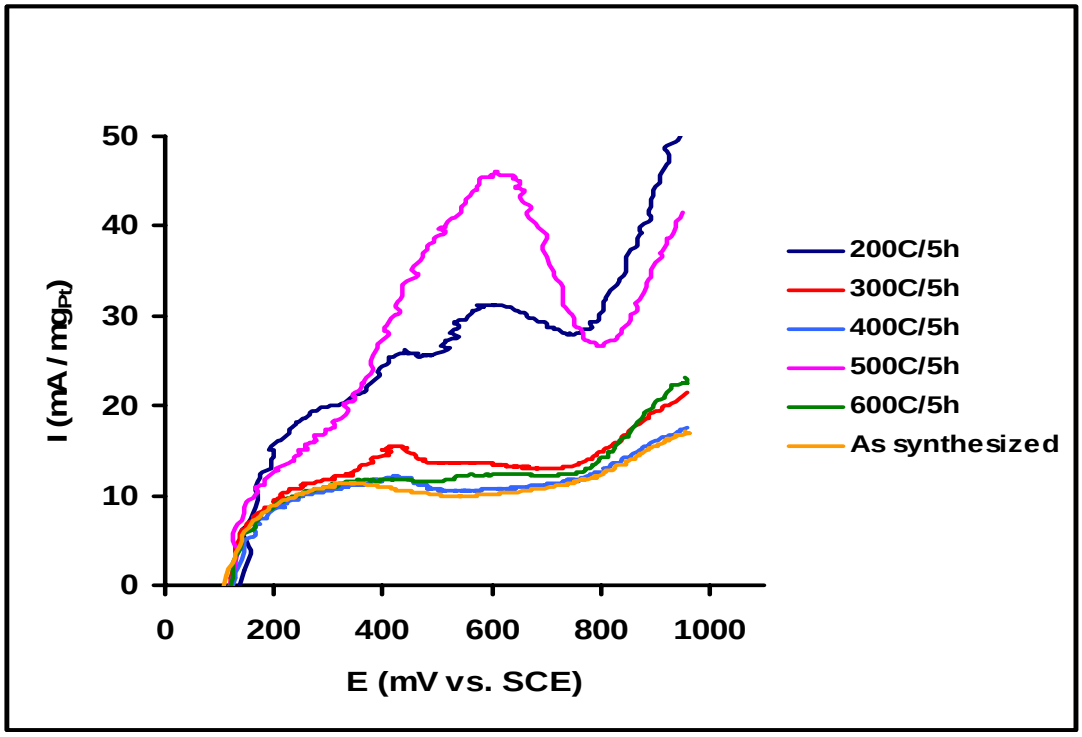

Figure 3.15. Cyclic voltammograms of thiol stabilized $Pt_{75}Ru_{25}$/C nanoparticle catalyst (1:1 thiol/PtRu molar ratio, heated up for 5 hours between 200-600°C) in 0.1 M $HClO_4$ + 0.4 M CH_3OH at room temperature. Scan rate is 50 mV/s.

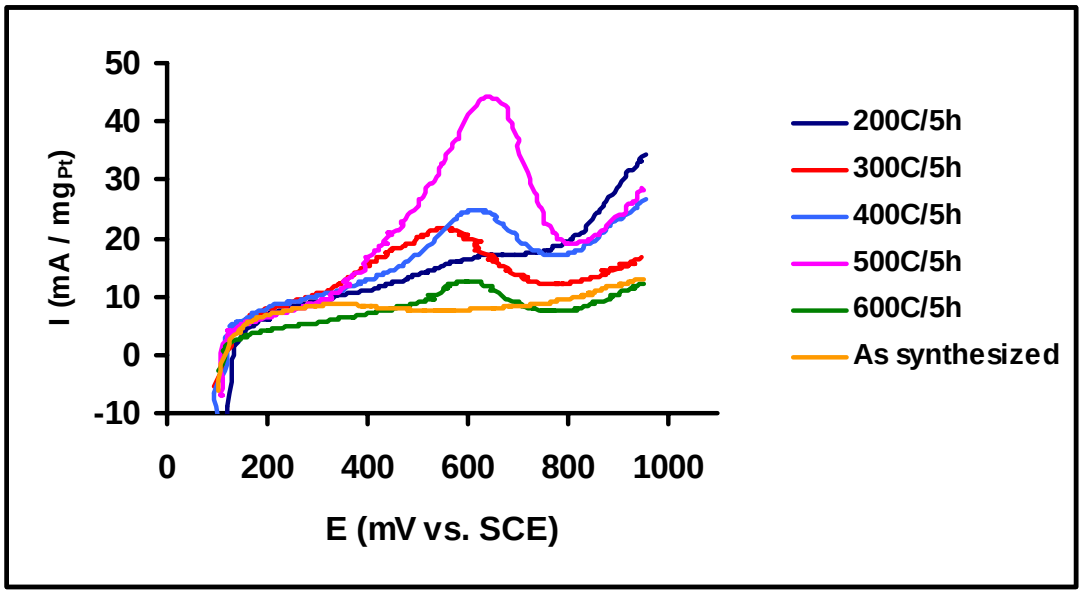

Figure 3.16. Cyclic voltammograms of thiol stabilized $Pt_{97}Ru_3$/C nanoparticle catalyst (1:1 thiol/PtRu molar ratio, heated up for 5 hours between 200-600^oC) in 0.1 M $HClO_4$ + 0.4 M CH_3OH at room temperature. Scan rate is 50 mV/s.

3.2. X-RAY DIFFRACTION AND TRANSMISSION ELECTRON MICROSCOPY

XRD and TEM techniques have been used in order to determine the average crystallite particle sizes. The average crystallite particle sizes of the crystallite specie can be found from powder diffraction data using the Scherrer formula;

$$L = k\lambda / (\beta_{1/2} \cos\theta)$$

where L is the effective crystallite diameter, k is a constant [taken to be 0.9 as recommended by Klug and Alexander (1962)], λ is the wavelenght of the incident X-rays, β is the breadth of a diffraction peak at half-height and θ is the position of the peak maximum. While line broadening is useful in determining the average particle size in systems with a narrow particle size distribution, it is of limited value where a wide range of particle sizes are present and in general will over estimate the particle size. The powder XRD pattern of carbon unsupported 1-hexanethiol stabilized Pt, $Pt_{75}Ru_{25}$ and $Pt_{97}Ru_3$ nanoparticle catalysts were similar and one of them was shown

in Figure 3.17. As clearly seen from the Figure, XRD pattern indicated no peaks corresponding to Pt and Ru due to small crystallite sizes of Pt and Ru metals.

Transmission electron microscopy enables the direct observation of individual crystallites and can provide both average particle size and the size distribution. In case of as synthesized 1-hexanethiol stabilized Pt/C nanoparticle catalyst sample, Figure 3.18, a relatively narrow range of particle sizes was observed by transmission electron micrographs. The particles appeared to be uniformly distributed on the carbon support and there was no evidence for agglomeration of the crystallites. The average particle size was found to be 3-5 nm. This was comparible to the size found for platinum crystallites, 3-4 nm, using microwave method (Liu et al., 2005) and, 4-5 nm, using microwave assisted polyol process (Liu et al., 2004). Transmission electron micrograph of the most active 1-hexanethiol stabilized Pt/C nanoparticle catalyst with 1:1 thiol/platinum molar ratio which was heated up at 200 ^{o}C for 5 hours was given in Figure 3.19. In this material, almost all particles were in the range of 8-10 nm diameter, and were uniformly distributed on the carbon support as in the previous case.

As given in the cyclic voltammetry section, temperature increase above 200 ^{o}C caused to decrease the activity of catalyst towards methanol oxidation reaction. The heating process might produce a sintering of small metal crystallites and cause to increase in average particle size. Increase in particle size would result in a lowering of the catalytic performance of the catalyst towards methanol oxidation reaction. The transmission electron micrograph of the least active catalyst, 1-hexanethiol stabilized Pt/C nanoparticle catalyst with 1:1 thiol/platinum molar ratio which was heated up at 400^{o}C for 5 hours, was also taken, Figure 3.20., and electron micrograph of this sample showed the presence of a small agglomerated particles with a size of 10-15 nm in diameter as expected.

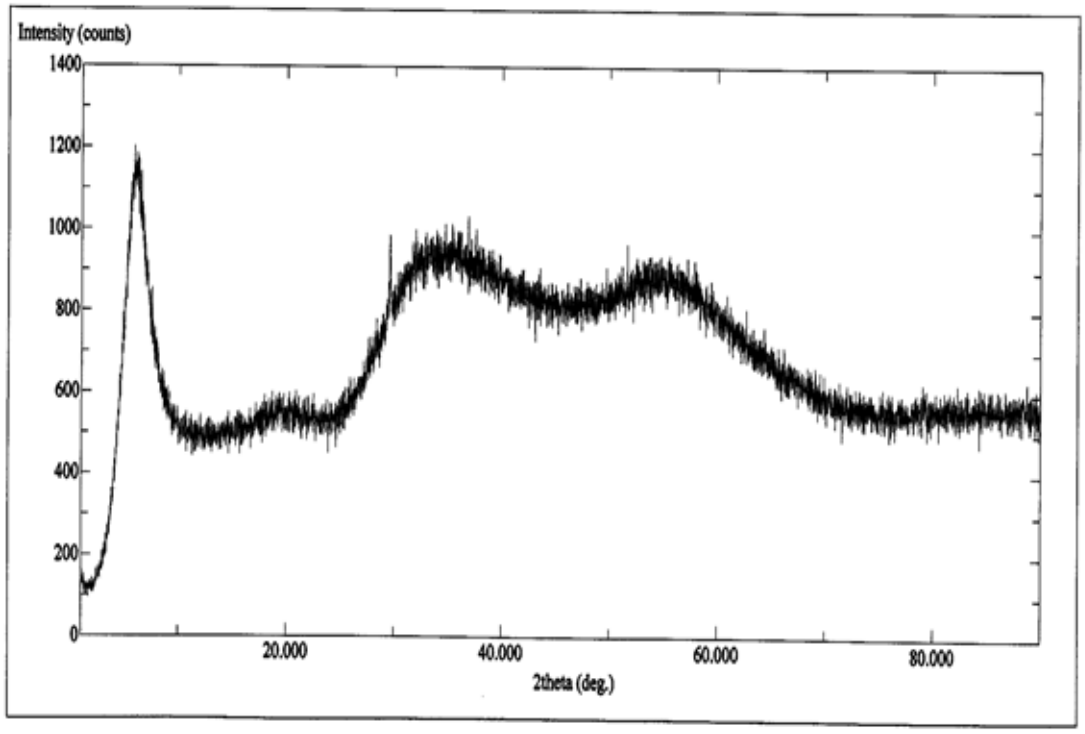

Figure 3.17. XRD pattern of carbon unsupported 1-hexanethiol stabilized $Pt_{75}Ru_{25}$ nanoparticle catalyst with 1:1 thiol/PtRu molar ratio.

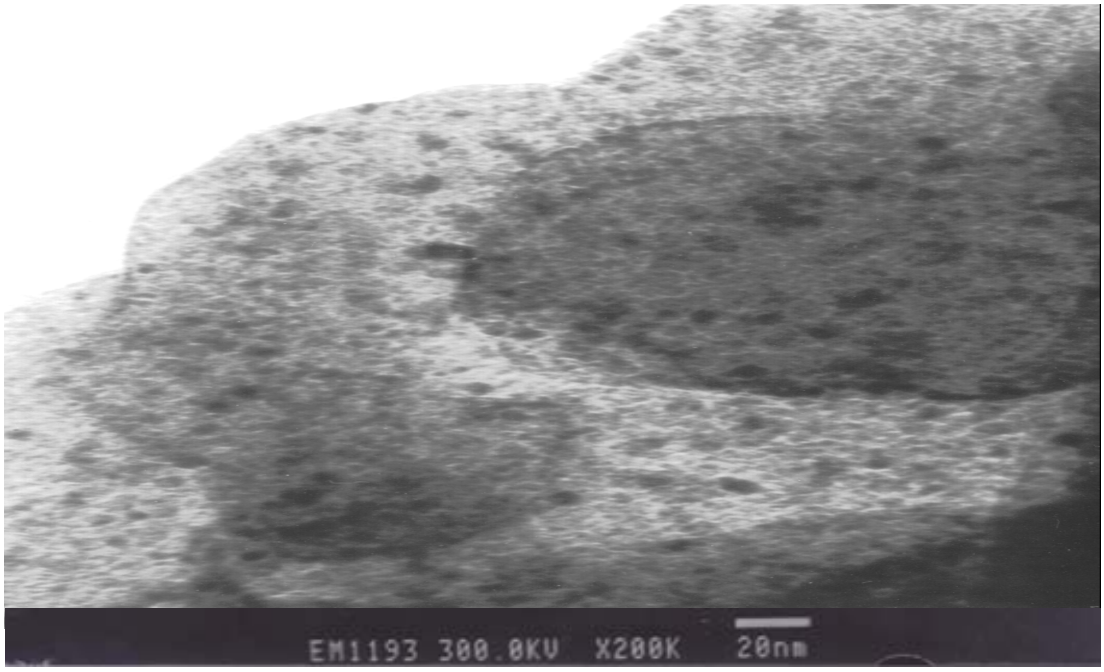

Figure 3.18. TEM image of as synthesized 1-hexanethiol stabilized Pt/C nanoparticle catalyst with 1:1 thiol/platinum molar ratio.

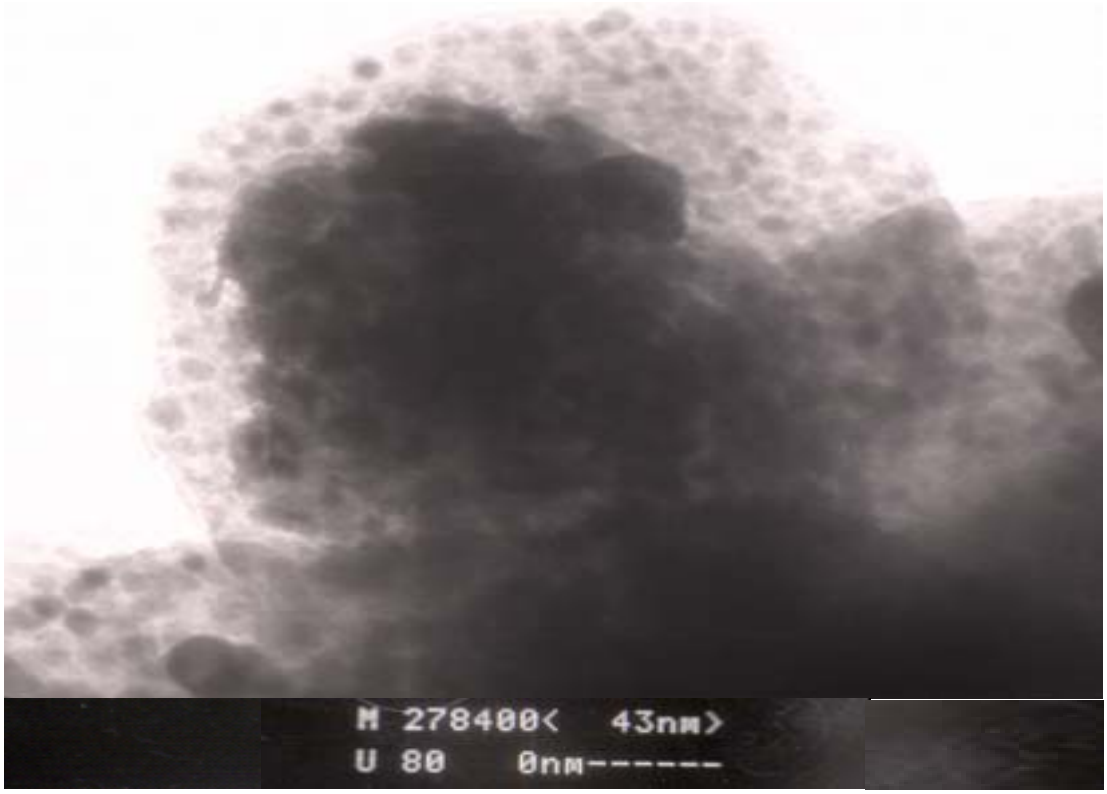

Figure 3.19. TEM image of 1-hexanethiol stabilized Pt/C nanoparticle catalyst (heated up at 200^{o}C for 5 hours) with 1:1 thiol/platinum molar ratio.

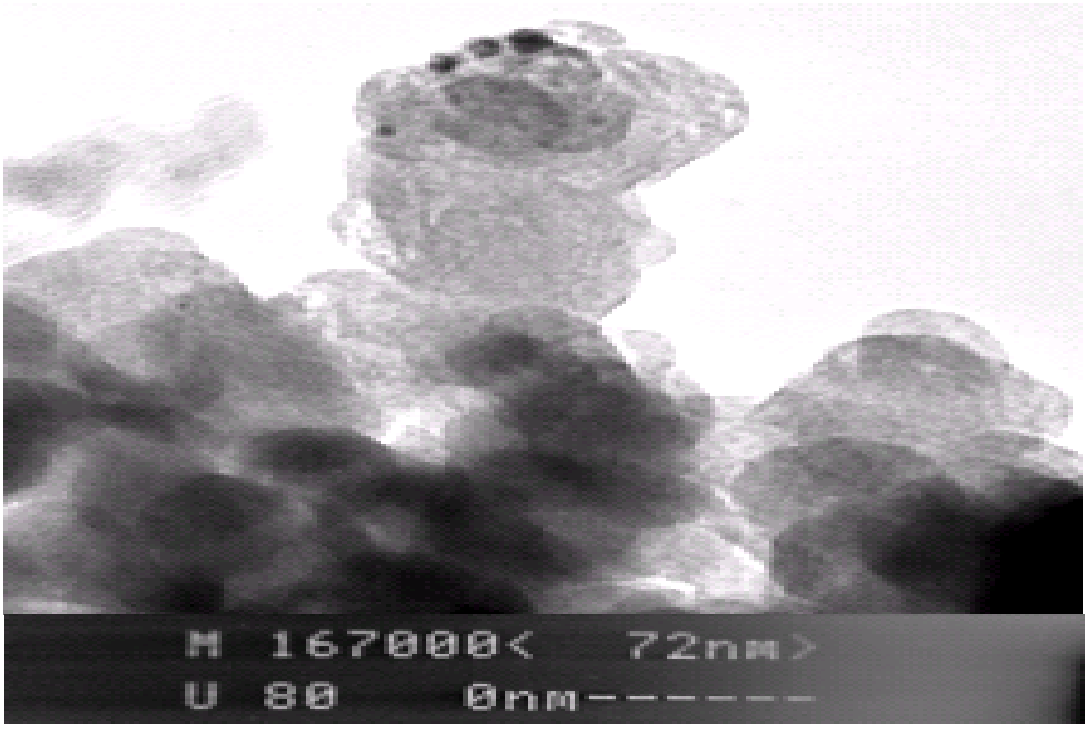

Figure 3.20. TEM image of 1-hexanethiol stabilized Pt/C nanoparticle catalyst (heated up at 400^{o}C for 5 hours) with 1:1 thiol/platinum molar ratio.

3.3. X-RAY PHOTOELECTRON SPECTROSCOPY

XPS technique has been used in order to obtain information about the composition, environment and relative surface concentrations of prepared catalysts. A low resolution wide range XP spectra of carbon unsupported 1-hexanethiol stabilized Pt, Ru, $Pt_{75}Ru_{25}$ and $Pt_{97}Ru_3$ nanoparticle catalysts with 1:1 thiol/metal molar ratio were shown in Figure 3.21., 3.22., 3.23. and 3.24., respectively. C 1s, O 1s, Pt 4f, Ru 3d and S 2p spectra were observed for these catalysts.

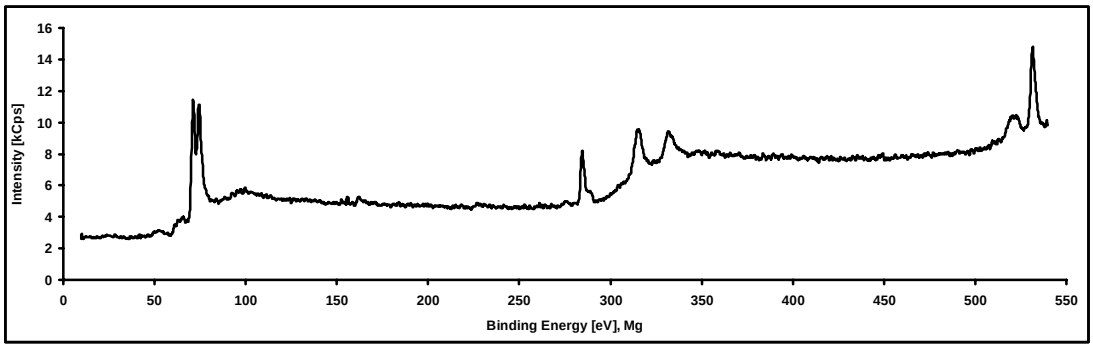

Figure 3.21. Wide range XPS spectra of as synthesized carbon unsupported 1-hexanethiol stabilized platinum nanoparticle catalyst with 1:1 thiol/platinum molar ratio.

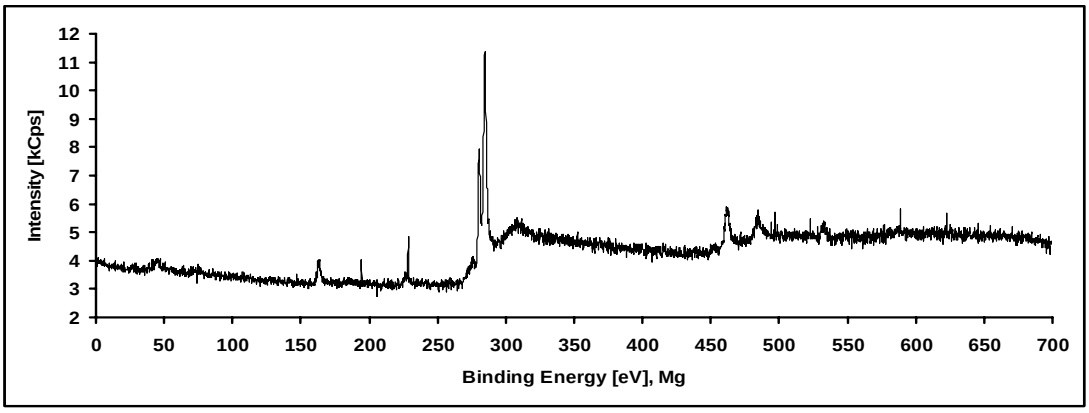

Figure 3.22. Wide range XPS spectra of as synthesized carbon unsupported 1-hexanethiol stabilized ruthenium nanoparticle catalyst with 1:1 thiol/ruthenium molar ratio.

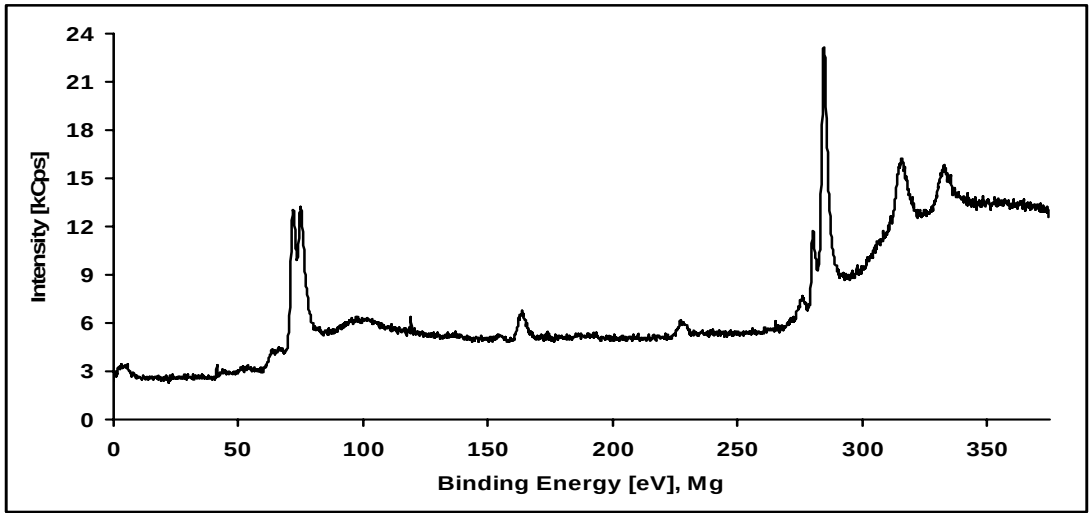

Figure 3.23. Wide range XPS spectra of as synthesized carbon unsupported 1-hexanethiol stabilized $Pt_{75}Ru_{25}$ nanoparticle catalyst with 1:1 thiol/PtRu molar ratio.

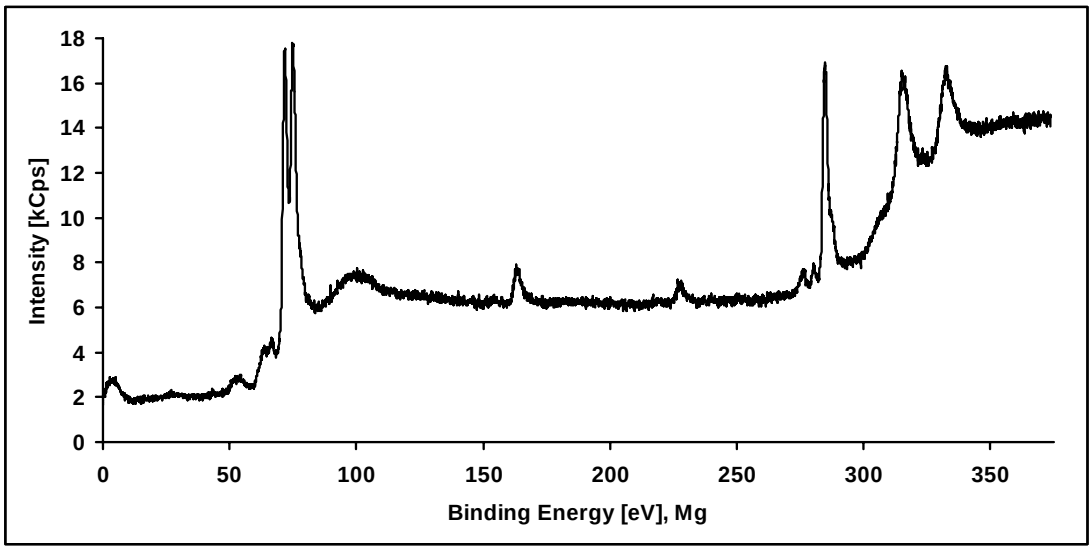

Figure 3.24. Wide range XPS spectra of as synthesized carbon unsupported 1-hexanethiol stabilized $Pt_{97}Ru_3$ nanoparticle catalyst with 1:1 thiol/PtRu molar ratio.

3.3.1. XPS RESULTS OF AS SYNTHESIZED CARBON UNSUPPORTED 1-HEXANETHIOL STABILIZED PLATINUM NANOPARTICLE CATALYST WITH 1:1 THIOL/PLATINUM MOLAR RATIO

C 1s, Pt 4f and S 2p regions of spectrum for 1-hexanethiol stabilized platinum nanoparticle catalyst were given in Figure 3.25., 3.26. and 3.27., respectively. The C 1s region consisted of a strong peak at 284.6 eV and weaker peaks at 286, 287.5 and 289.2 eV, Figure 3.25. The peaks at high bonding energy values was thought to be higher oxidation state of carbon, such as C=O, O=C–OH or C–OH (Gökağaç, 1993a).

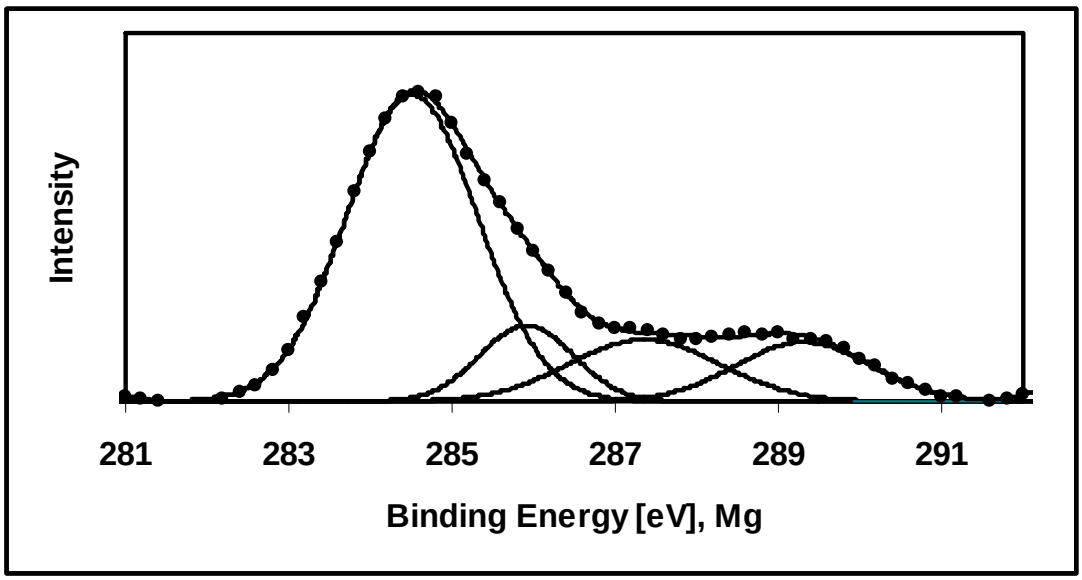

Figure 3.25. Fitted C 1s electron spectra of as synthesized carbon unsupported 1-hexanethiol stabilized platinum nanoparticle catalyst with 1:1 thiol/platinum molar ratio.

The Pt 4f electron spectra of carbon unsupported thiol stabilized platinum nanoparticle catalyst was shown in Figure 3.26. Three well resolved doublets were observed by a Gaussian - Lorentzian spectral fitting, which indicated that three kinds

of platinum specie must be present on the surface of prepared catalyst. The bulk of the platinum was present as Pt(0), Pt $4f_{7/2}$ binding energy of 71.2 and Pt $4f_{5/2}$ binding energy of 74.4 eV (Liu et al., 2005), with a certain amount of oxidized platinum, Pt $4f_{7/2}$ binding energy of 72.4 and Pt $4f_{5/2}$ binding energy of 75.7 eV, and a small amount of another platinum oxide species, Pt $4f_{7/2}$ binding energy of 76.7 and Pt $4f_{5/2}$ binding energy of 79.1 eV.

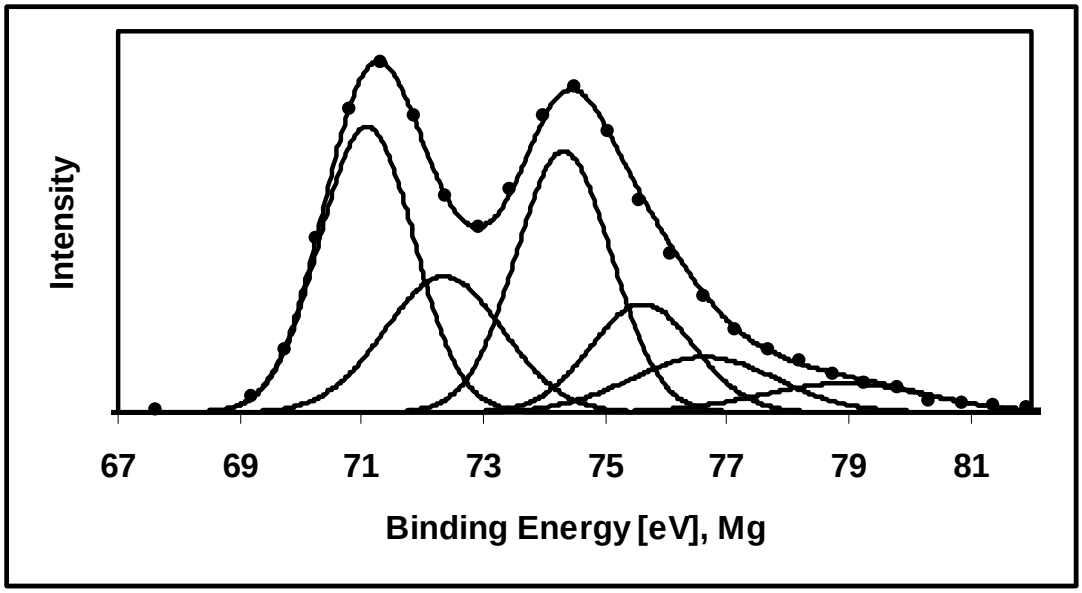

Figure 3.26. Fitted Pt 4f electron spectra of as synthesized carbon unsupported 1-hexanethiol stabilized platinum nanoparticle catalyst with 1:1 thiol/platinum molar ratio.

The binding energy of Pt(II) species was less established, since it was not possible to isolate stable bulk samples of a Pt(II) oxide or hydroxide. Nevertheless, it appeared that Pt(II) species have Pt $4f_{7/2}$ binding energy of 72.5 - 73.8 eV (Watanabe et al., 1987). There was also an evidence that the Pt binding energy shifts upon formation of species such a PtO_{ads} to 72.1 – 72.2 eV (Watanabe et al., 1987). The current catalyst binding energy of oxidized species was indicative of Pt(II), although the exact nature of this species was uncertain.

The least intense lines at 76.7 and 79.1 eV might be due to a higher oxidation state of Pt, presumably Pt(IV). This value was much higher than the predicted one, such as previously, it has been shown that Pt $4f_{7/2}$ binding energies for $Pt(OH)_4$ is 74.4 eV (Goodenough et al., 1988) and for PtO_2 is 74.6 – 74.9 eV (Watanabe et al., 1987). Deviation from simple doublet values might be explained by screening of core electron by the conduction electron would give rise to assymmetric peak shapes.

The observation of very weak S $2p_{3/2}$ and $2p_{1/2}$ peak at 161.8 and 163 eV showed the presence of small amount of surfactant on the surface of the catalyst as shown in Figure 3.27. This values belonged to surface-bound sulfur on Pt (Li et al., 2003). This result indicated that platinum nanoparticle surface was not perfectly cleaned by washing process.

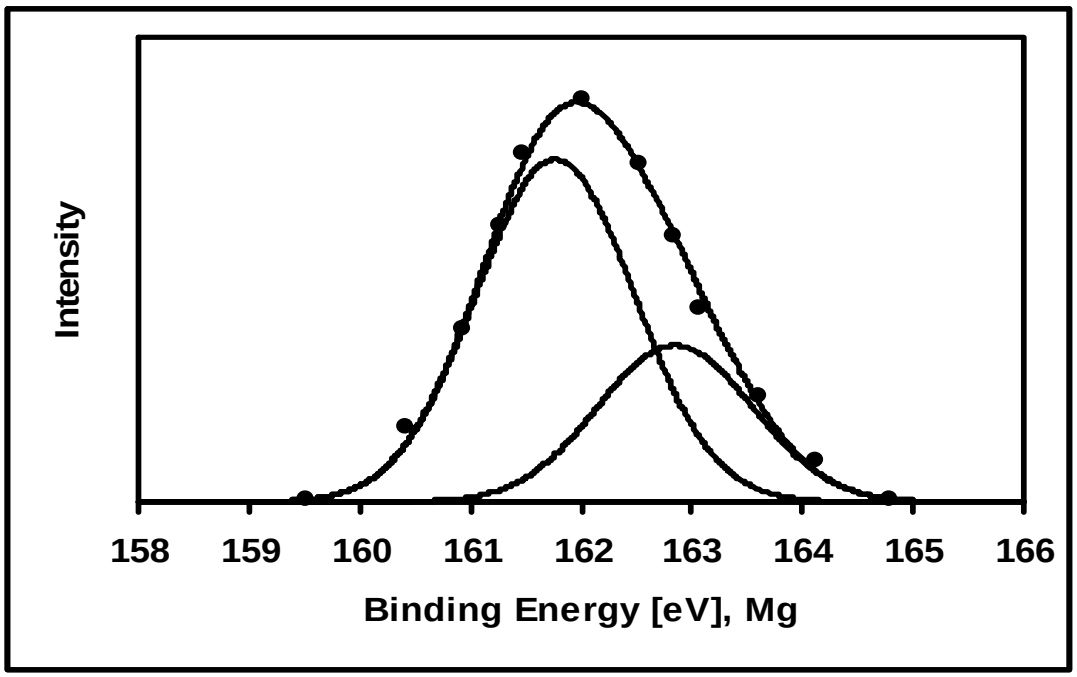

Figure 3.27. Fitted S 2p electron spectra of as synthesized carbon unsupported 1-hexanethiol stabilized platinum nanoparticle catalyst with 1:1 thiol/platinum molar ratio.

3.3.2. XPS RESULTS OF AS SYNTHESIZED CARBON UNSUPPORTED 1-HEXANETHIOL STABILIZED RUTHENIUM NANOPARTICLE CATALYST WITH 1:1 THIOL/RUTHENIUM MOLAR RATIO

XP spectra of 1-hexanethiol stabilized ruthenium nanoparticle catalyst with 1:1 thiol/ruthenium molar ratio was also taken in order to compare its $3d_{5/2}$ binding energy values with 1-hexanethiol stabilized Pt + Ru catalysts. The Ru $3d_{5/2}$ region of spectra was shown in Figure 3.28. The C 1s line was at approximately the same binding energy as that of the diagnostic Ru 3d line, limiting the ability to observe the highly oxidized Ru species by XPS. On the other hand, the Ru 3d line is typically broad and insensitive to changes in the ruthenium oxide state.

The use of mixed Gaussian - Lorentzian shaped lines of C 1s signal of as prepared material indicated the presence of two singlets with an intense C 1s binding energy of 284.8 eV which can be used as a reference point for XP spectrum and a weak C 1s binding energy of 287.7 eV which might be due to higher oxidation state of carbon such as C=O, O=C–OH or C–OH species (Gökağaç, 1993a).

In the present work, it appeared that two ruthenium specie were present. The binding energy of the stronger of these, Ru $3d_{5/2}$ binding energy of 280.4 eV, indicated that Ru was in zero oxidation state, consistent with the Ru $3d_{5/2}$ line in Ru(0) was 280 eV (Kim and Winograd, 1974). The second Ru $3d_{5/2}$ line at 281.4 eV indicated presence of ruthenium oxide, Ru(IV), as observed in $Bi_2Ru_2O_7$ at 281.5 eV (Gökağaç and Kennedy, 1993b).

Three different types of sulfur were obtained by three S $2p_{3/2}$ - $2p_{1/2}$ doublets at 161.2-162.5 eV, 162.6-163.6 eV and 163.2-164.5 eV for this catalyst as shown in Figure 3.29. The first doublet might be due to covalently bound sulfur species, 1-hexanethiol, on the Pt surface ($R{-}SH + Pt \rightarrow R{-}S{-}Pt + ½\ H_2$) while the second and third doublets might represent unbound sulfur specie on the Pt surface, 1-hexanethiol and surfactant dimer (Li et al., 2003). As it was explained previously, these peaks came from surfactant, 1-hexanethiol, which was used at the preparation step and it was very difficult to remove those surfactants from the surface of ruthenium nanoparticles.

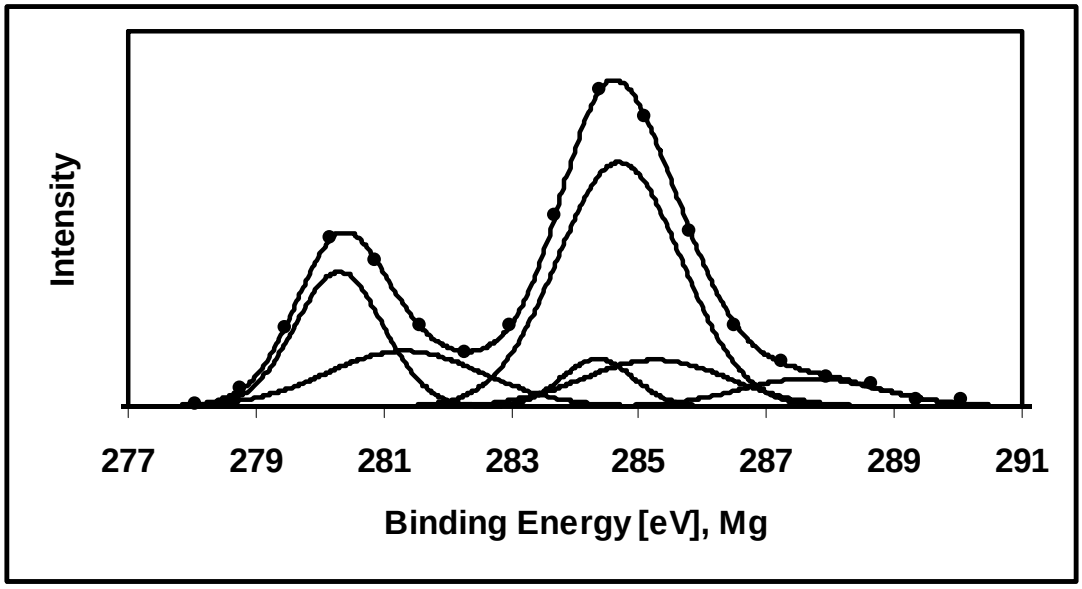

Figure 3.28. Fitted Ru 3d electron spectra of as synthesized carbon unsupported 1-hexanethiol stabilized ruthenium nanoparticle catalyst with 1:1 thiol/ruthenium molar ratio.

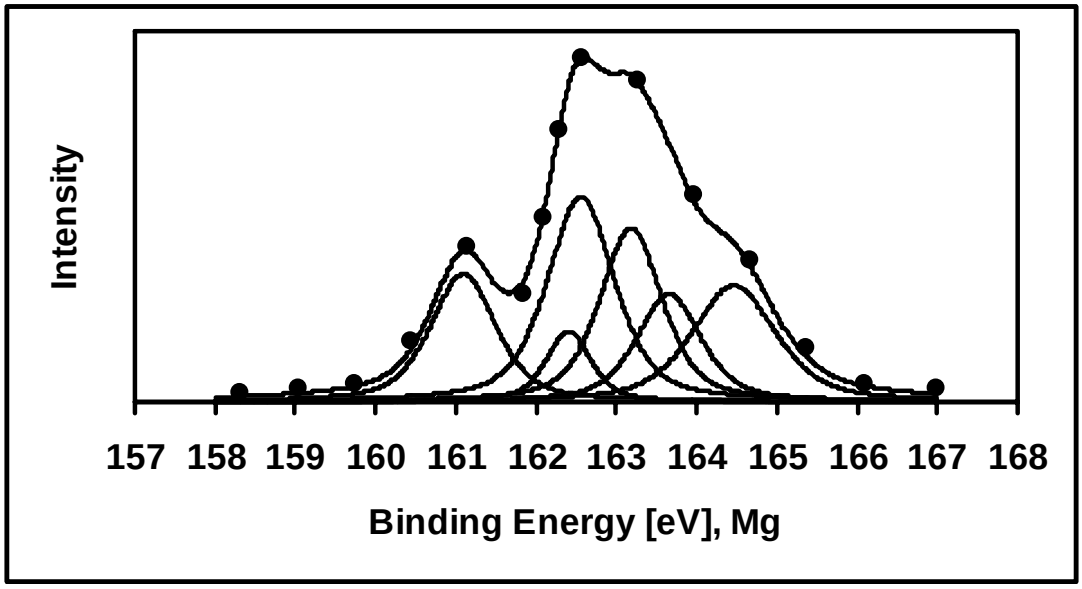

Figure 3.29. Fitted S 2p electron spectra of as synthesized carbon unsupported 1-hexanethiol stabilized ruthenium nanoparticle catalyst with 1:1 thiol/ruthenium molar ratio.

3.3.3. XPS RESULTS OF AS SYNTHESIZED CARBON UNSUPPORTED 1-HEXANETHIOL STABILIZED $Pt_{75}Ru_{25}$ AND $Pt_{97}Ru_3$ NANOPARTICLE CATALYSTS WITH 1:1 THIOL/PtRu MOLAR RATIO

XP spectrum of carbon unsupported 1-hexanethiol stabilized $Pt_{75}Ru_{25}$ and $Pt_{97}Ru_3$ nanoparticle catalysts with 1:1 thiol/PtRu molar ratio were also recorded and Pt $4f_{7/2}$, Ru $3d_{5/2}$ and S 2p regions of spectrum were given in Figure 3.30, 3.31., 3.32., 3.33., 3.34. and 3.35. Also, binding energy values of different oxidation states of Pt and Ru in these catalysts were tabulated in Table 3.2.

The Pt $4f_{7/2}$ spectrum revealed three doublets in both cases due to Pt(0), Pt(II) and Pt(IV) oxidation states, as observed for carbon unsupported 1-hexanethiol stabilized platinum nanoparticle catalyst, Figure 3.30. and 3.31. The binding energies of Pt(0) 4f spectra of $Pt_{75}Ru_{25}$ nanoparticle catalyst ($4f_{7/2}$ BE = 71.8 eV, $4f_{5/2}$ BE = 75.1 eV) was higher than that found for either bulk Pt ($4f_{7/2}$ BE = 71.1 eV, $4f_{5/2}$ BE = 74.4 eV) (Liu et al., 2005) and currently prepared Pt nanoparticle catalyst in this study ($4f_{7/2}$ BE = 71.2 eV, $4f_{5/2}$ BE = 74.4 eV). This positive shift corresponds to a decrease in the electronic charge density on the Pt atoms present in the $Pt_{75}Ru_{25}$ nanoparticle catalyst. Small but similar type of shift was observed for $Pt_{97}Ru_3$ nanoparticle catalyst, binding energy of Pt $4f_{7/2}$ BE = 71.6 eV, Pt $4f_{5/2}$ BE = 75.1 eV. The dependence of peak position of Pt(0) $4f_{7/2}$ may indicate that Ru atoms are strong electron withdrawing in the mixed Pt + Ru species or Pt/Ru alloy. It was not surprising that the same trend was not observed for +2 and +4 oxidation states of Pt; because, they do not form Pt/Ru alloy or Pt/Ru crystallite, they are platinum oxide specie. The Pt(IV) specie have $4f_{7/2}$ binding energies of 74.3 and 74.9 eV for $Pt_{75}Ru_{25}$ and $Pt_{97}Ru_3$ nanoparticle catalysts, respectively. These results were consistent with $Pt(OH)_4$ $4f_{7/2}$ BE = 74.4 eV (Goodenough et al., 1988) and PtO_2 $4f_{7/2}$ BE = 74.6 - 74.9 eV (Watanabe et al., 1987). No doubt about the peak position of Pt(II) $4f_{7/2}$ binding energy values of $Pt_{75}Ru_{25}$ and $Pt_{97}Ru_3$ nanoparticle catalysts.

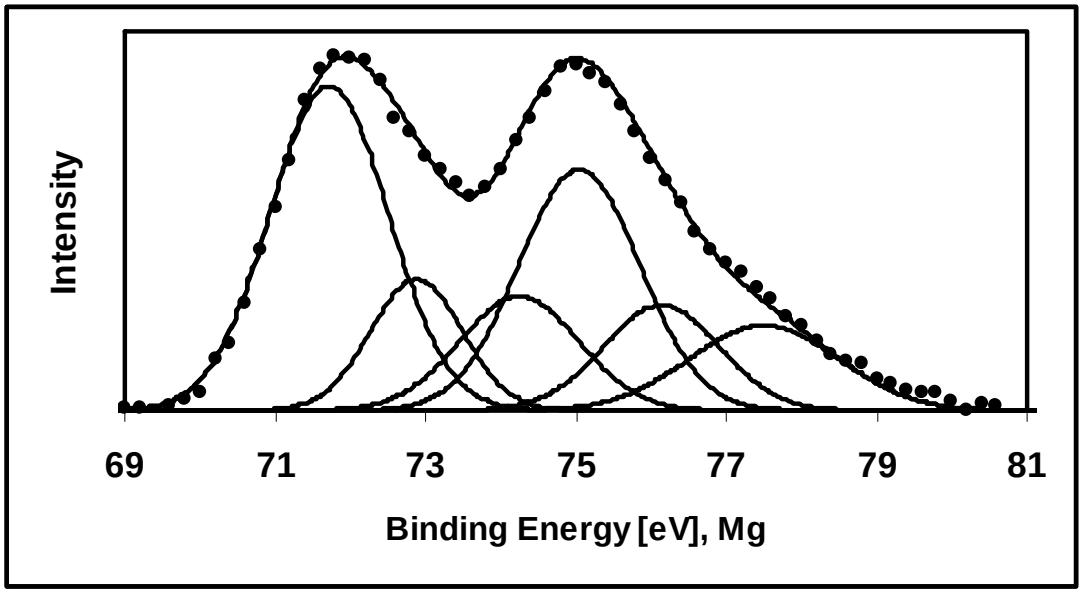

Figure 3.30. Fitted Pt 4f electron spectra of as synthesized carbon unsupported 1-hexanethiol stabilized $Pt_{75}Ru_{25}$ nanoparticle catalyst with 1:1 thiol/PtRu molar ratio.

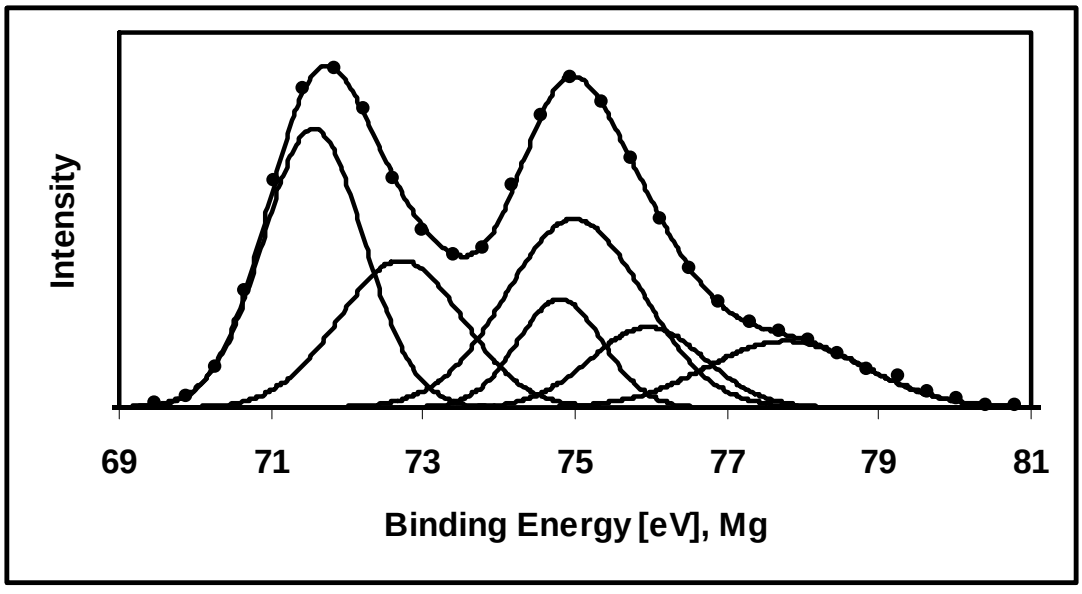

Figure 3.31. Fitted Pt 4f electron spectra of as synthesized carbon unsupported 1-hexanethiol stabilized $Pt_{97}Ru_3$ nanoparticle catalyst with 1:1 thiol/PtRu molar ratio.

Analysis of C 1s and Ru 3d region of XP spectra of $Pt_{75}Ru_{25}$ nanoparticle catalyst showed similar trend as in Ru nanoparticle catalyst but with low intensities, Figure 3.32. Basically, two types of Ru specie were observed, Ru(0) $3d_{5/2}$ binding energy of 280.3 and Ru(IV) $3d_{5/2}$ binding energy of 281.3 eV as noticed in Ru nanoparticle catalyst. The major difference between C 1s and Ru 3d regions of Ru, $Pt_{75}Ru_{25}$ and $Pt_{97}Ru_3$ nanoparticle catalysts was due to change in amount of Ru percent on the surface of catalysts. As given in the formula, the Pt/Ru ratios were 75/25 and 97/3 for $Pt_{75}Ru_{25}$ and $Pt_{97}Ru_3$ nanoparticle catalyst, respectively. Only Ru(0), $3d_{5/2}$ binding energy of 280.3 eV, was observed for $Pt_{97}Ru_3$ catalyst, Figure 3.33. However, this does not mean there was no high oxidation state of ruthenium. The absence of this feature might be due to presence of very small amount of high oxidation state of ruthenium, which was difficult to detect in the spectra.

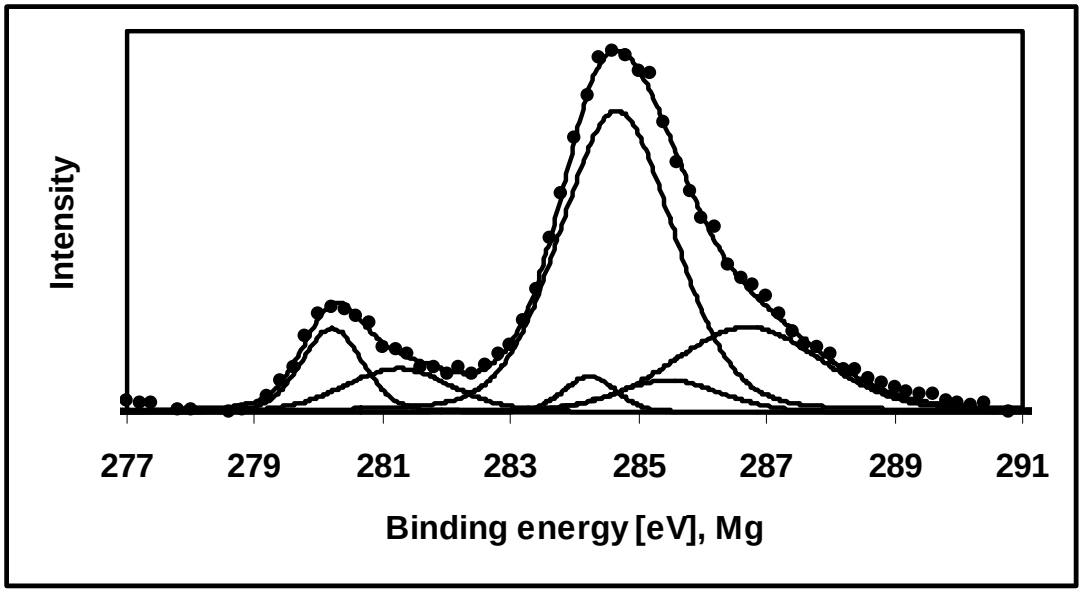

Figure 3.32. Fitted Ru 3d electron spectra of as synthesized carbon unsupported 1-hexanethiol stabilized $Pt_{75}Ru_{25}$ nanoparticle catalyst with 1:1 thiol/PtRu molar ratio.

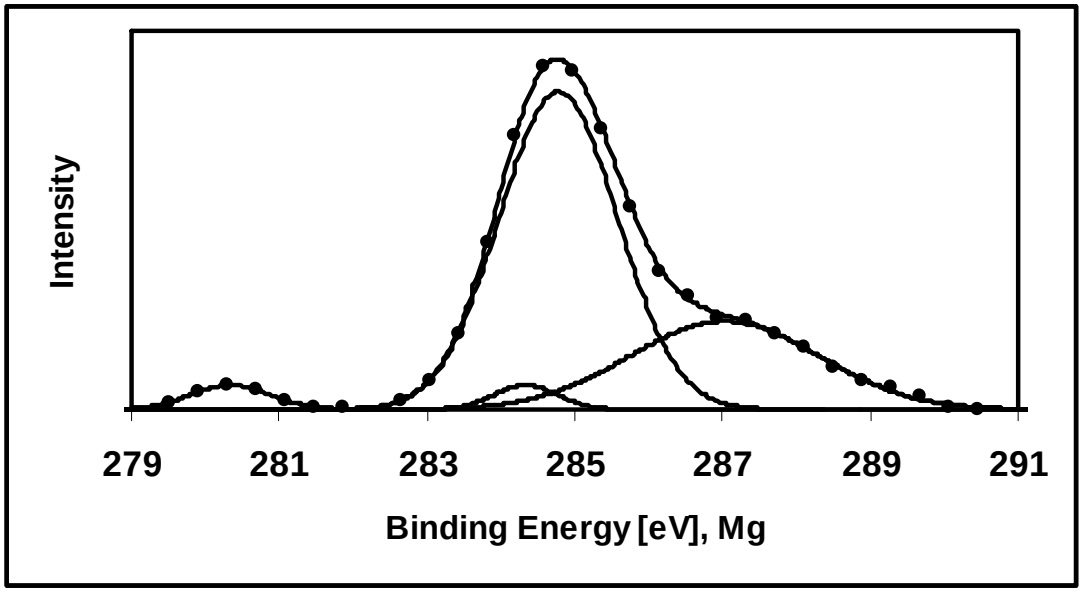

Figure 3.33. Fitted Ru 3d electron spectra of as synthesized carbon unsupported 1-hexanethiol stabilized $Pt_{97}Ru_3$ nanoparticle catalyst with 1:1 thiol/PtRu molar ratio.

Two S $2p_{3/2}$ and $2p_{1/2}$ doublets were observed for both carbon unsupported $Pt_{75}Ru_{25}$ and $Pt_{97}Ru_3$ nanoparticle catalysts due to two different kinds of sulfur. The binding energy values of doublets were 162.5-163.6 and 164.1-165.4 eV for $Pt_{75}Ru_{25}$, 162.2-163.7 and 163.3-164.7 eV for $Pt_{97}Ru_3$ nanoparticle catalysts, Figure 3.34. and 3.35. The first doublets of each catalyst might be due to covalently bound sulfur species on the platinum surface while the second doublets might represent unbound sulfur species, as described in Section 3.3.2. (Li et al., 2003). The peaks existed due to unremoved surfactant molecules on the surface of metal nanoparticles.

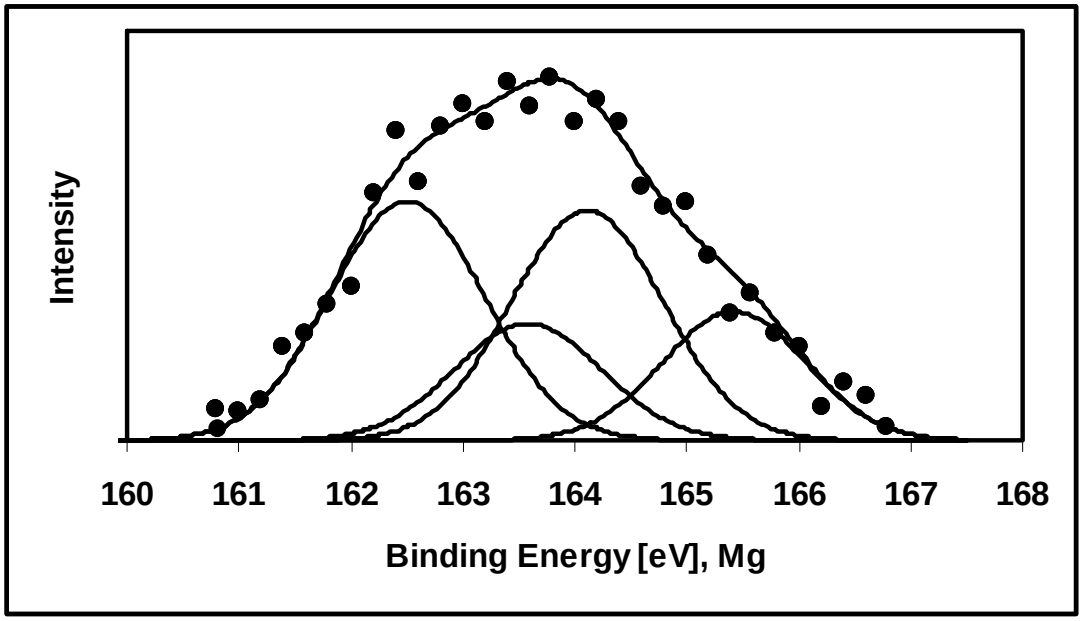

Figure 3.34. Fitted S 2p electron spectra of as synthesized carbon unsupported 1-hexanethiol stabilized $Pt_{75}Ru_{25}$ nanoparticle catalyst with 1:1 thiol/PtRu molar ratio.

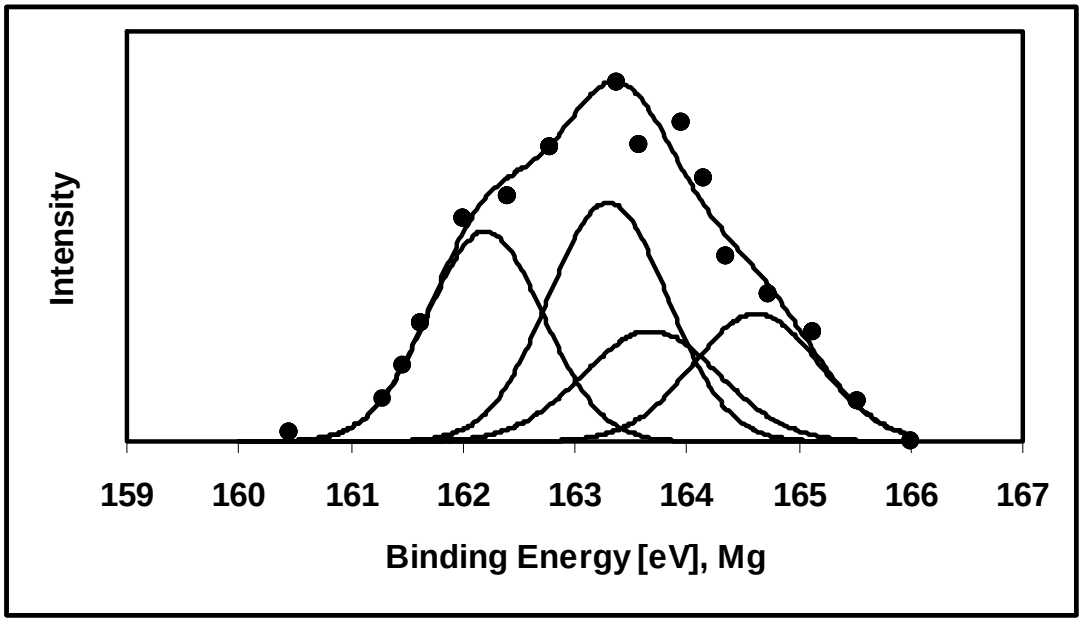

Figure 3.35. Fitted S 2p electron spectra of as synthesized carbon unsupported 1-hexanethiol stabilized $Pt_{97}Ru_3$ nanoparticle catalyst with 1:1 thiol/PtRu molar ratio.

Table 3.2. Fitted Pt $4f_{7/2}$ - $4f_{5/2}$ and Ru $3d_{5/2}$ - $3d_{3/2}$ binding energy values, eV, for carbon unsupported 1-hexanethiol stabilized Pt, Ru, $Pt_{75}Ru_{25}$ and $Pt_{97}Ru_3$ nanoparticle cataysts with 1:1 thiol/metal molar ratio.

Samples	Pt(0)	Pt(II)	Pt(IV)	Ru(0)	Ru(IV)
1-hexanethiol stabilized Pt nanoparticle catalyst	71.2 ($4f_{7/2}$) 74.4 ($4f_{5/2}$)	72.4 ($4f_{7/2}$) 75.7 ($4f_{5/2}$)	76.7 ($4f_{7/2}$) 79.1 ($4f_{5/2}$)	–	–
1-hexanethiol stabilized Ru nanoparticle catalyst	–	–	–	280.4 ($3d_{5/2}$) 284.4 ($3d_{3/2}$)	281.4 ($3d_{5/2}$) 285.4 ($3d_{3/2}$)
1-hexanethiol stabilized $Pt_{75}Ru_{25}$ nanoparticle catalyst	71.8 ($4f_{7/2}$) 75.1 ($4f_{5/2}$)	72.9 ($4f_{7/2}$) 76.2 ($4f_{5/2}$)	74.3 ($4f_{7/2}$) 77.5 ($4f_{5/2}$)	280.3 ($3d_{5/2}$) 284.3 ($3d_{3/2}$)	281.3 ($3d_{5/2}$) 285.3 ($3d_{3/2}$)
1-hexanethiol stabilized $Pt_{97}Ru_3$ nanoparticle catalyst	71.6 ($4f_{7/2}$) 75.1 ($4f_{5/2}$)	72.3 ($4f_{7/2}$) 76.1 ($4f_{5/2}$)	74.9 ($4f_{7/2}$) 77.9 ($4f_{5/2}$)	280.3 ($3d_{5/2}$) 284.4 ($3d_{3/2}$)	–

CHAPTER IV

CONCLUSION

Cyclic voltammetry, transmission electron microscopy, X-ray diffraction, X-ray photoelectron spectroscopy results showed that particle size distribution, surface composition, oxidation state of metals and metal-metal interactions were all important parameters contributing to the activity of the carbon supported 1-hexanethiol stabilized Pt, $Pt_{75}Ru_{25}$ and $Pt_{97}Ru_3$ catalysts for electrooxidation of methanol. Electrochemical studies demonstrated that carbon supported 1-hexanethiol stabilized Pt which was heated up at 200^{o}C for 5 hours had the highest catalytic activity for methanol oxidation reaction and transmission electron micrographs of this catalyst showed that all platinum nanoparticles were between 8-10 nm diameter and uniformly distributed on carbon support.

Carbon supported 1-hexanethiol stabilized $Pt_{75}Ru_{25}$ and $Pt_{97}Ru_3$ were poor catalysts for direct electrooxidation of methanol due to unremoved stabilizer, 1-hexanethiol, shell around the Pt/Ru nanoparticles and coverage of Pt by Ru, which decreased the active surface area of Pt nanoparticles.

The Ru 3d electron spectra of carbon unsupported $Pt_{75}Ru_{25}$ consisted of two doublets with Ru $3d_{5/2}$ indicative of Ru(0) and Ru(IV), while $Pt_{97}Ru_3$ was a simple doublet with Ru(0). The Pt 4f electron spectrum of all the catalysts were found in three different oxidation states, namely Pt(0), Pt(II) and Pt(IV). Pt(0) binding energy values (71.8 eV and 71.6 eV) for $Pt_{75}Ru_{25}$ and $Pt_{97}Ru_3$ catalysts were noticeably

higher than that found for other carbon supported platinum samples, 71.0 eV, as a consequence of a decrease in charge density on the platinum atoms.

There are two possible pathways for the reaction of a metal oxide, $Pt–OH_2$, with the adsorbed methanol residue, $Pt_3–C–OH$, during methanol oxidation reaction. The ruthenium oxide can react either directly with the adsorbed methanol residue or it can promote the formation of an active platinum oxide which subsequently completes the methanol oxidation reaction. In case of both carbon supported 1-hexanethiol stabilized Pt/Ru electrodes, both mechanism were not valid, because of existence of stabilizer on the surface of Pt + Ru nanoparticles, which prevent reaction between metal oxide and methanol residue during methanol oxidation reaction.

REFERENCES

Adzic, R.R., *Israel Journal of Chemistry*, 18, 166, 1979.

Bacon, F.T., Chapter 5, ed. Young, G.J., Fuel Cells, Vol.1, Reinhold Publishing Corporation, New York, 1960.

Bagotzky, V.S. and Vassiliev, Yu.B., *Electrochimica Acta*, 12, 1323, 1967.

Bagotzky, V.S., Vassiliev, Yu.B., and Khazova, O.A., *Journal of Electroanalytical Chemistry*, 81, 229, 1977.

Bard, A.J., Parsons, R., and Jordan, J., *Standart Potentials in Aqueous Solutions*, Marcel Dekker, New York, 1985.

Baur, E. and Preis, H., *Zeitschrift für Electrochemie*, 43, 727, 1937.

Beden, B., Kadirgan, F., Lamy, C., and Leger J.M., *Journal of Electroanalytical Chemistry*, 127, 75, 1981.

Biegler, T. and Koch, D.F.A., *Journal of the Electrochemical Society*, 114, 904, 1967.

Biegler, T., *Australian Journal of Chemistry*, 26, 2571, 1973.

Bockris, J.O'M. and Srinivasan, S., *Fuel Cells – Their Electrochemistry*, McGraw Hill, New York, 1969.

Bockris, J.O'M., Conway, B. E., Yeager, E., and White, R. R., *Comprehensive Treatise of Electrochemistry*, 3, Electrochemical Energy Conversion and Storage, Plenum Press, New York, 1981.

Brust, M., Walker, M., Bethell, D., Schiffrin, D.J., and Whyman, R., *Journal of the Chemical Society, Chemical Communications*, 801, 1994.

Cathro, K.J. and Weeks C.H., *Energy Conversion*, 11, 143, 1971.

Davytan, O.K., *Bull. Acad. Sci.USSR, Classe Sci. Tech.*, 107, 125, 1946.

Goodenough, J.B., Hamnett, A., Kennedy, B.J., Manoharan, R., and Weeks, S.A., *Journal of Electroanalytical Chemistry*, 240, 133, 1988.

Goodenough, J.B., Manoharan, R., and Paranthaman, M., *Journal of the American Chemical Society*, 112, 2076, 1990.

Gökağaç, G., Metal Oxides as Promoters for Methanol Oxidation, Doctor of Philosophy Thesis in Chemistry, Univerity of Sydney, Australia, 1993a.

Gökağaç,G. and Kennedy, B.J., *Langmuir*, 9, 1862, 1993b.

Gökağaç, G., Leger, J.M., and Hahn, F., *Z. Naturforsch*, 56 b, 1306, 2001.

Grano, S.R., Cnossen, H., Skinner, W., Prestidge, C.A., and Ralston, J., *International Journal of Mineral Processing*, 50, 27, 1997.

Grove, W.R., *Philosophical Magazine and Journal of Science*, 14, 127, 1839.

Haber, F. and Brünner, R., *Zeitschrift für Elektrotechnik und Electrochemie*, 10, 697, 1904.

Haber, F. and Brünner, R., *Zeitschrift für Elektrotechnik und Electrochemie*, 12, 78, 1906.

Hamnett, A., Christensen, P.A., Kennedy, B.J., and Weeks, S.A., *E.E.C. Periodic Report*, Dec., 1987.

Hamnett, A. and Kennedy, B.J., *Electrochimica Acta*, 33, 1613, 1988.

Hamnett, A., Kennedy, B.J., and Wagner, F.E., *Journal of Catalysis*, 124, 30, 1990.

Hampson, N.A. and Willars, M.J., *Journal of Power Sources*, 4, 191, 1979.

Hoogers, G., Fuel Cell Technology Handbook, Boca Raton, Fla.: CRC Press, c2003.

Jacques W.W., *Zeitschrift für Elektrotechnik und Electrochemie*, 4, 129, 1897.

Katayama, A., *Journal of Physical Chemistry*, 84, 376, 1980.

Kazarinov, V. E., Tysyachnaya, G. Ya., and Andreev, V. N., *Journal of Electroanaytical Chemistry*, 65, 391, 1975.

Ketelaar, J.A. and Broers G.H.J., Chapter 6, ed. Young, G.J., Fuel Cells, Vol.1, Reinhold Publishing Corporation, New York, 1960.

Kim, K.S. and Winograd, N., *Journal of Catalysis*, 35, 66, 1974.

Kinoshita, K. and Stonehart, P., *Modern Aspects of Electrochemistry*, Vol.12, Bockris , J.O'M. and Conway, B.E., Eds., Plenum Press, New York, 1977, p. 183.

Klug, H. and Alexander, L., *X-ray Diffraction Procedures*, Wiley, New York, 1962.

Li, Z., Chang, S.C., and Williams, R.S., *Langmuir*, 19, 6744, 2003.

Liebhavskky, H.A. and Cairns, E.J., *Fuel Cells and Fuel Batteries*, Wiley, New York, 1968.

Liu, Z., Ling, X.Y., Su, X., and Lee, J.Y., *Journal of Physical Chemistry B*, 108, 8234, 2004.

Liu, Z., Gan, L. M., Hong, L., Chen, W., and Lee, J.Y., *Journal of Power Sources*, 139, 73, 2005.

McNicol, B. D. and Short, R.T., J*ournal of Electroanalytical Chemistry*, 81, 249, 1977.

McNicol, B. D., *Catalysis*, 2, 243, 1978.

McNicol, B.D., *Journal of Electroanalytical Chemistry*, 118, 71, 1981.

Mond, L. and Langer, C., *Proceedings of the Royal Society of London*, 46, 296, 1889.

Ostwald, W., *Zeitschrift für Elektrotechnik und Electrochemie*, 1, 122, 1894.

Schlatter, M.J., *Fuel Cells*, ed. Young G.J., 2, Reinhold Publishing Corporation, New York, 1963, p.190.

Vielstich, W., *Modern Process for the Electrochemical Production Energy*, Wiley Interscience, U.K., 1970a.

Vielstich, W., *Fuel Cells: Modern Processes for the Electrochemical Production of Energy*, Wiley Interscience, 1970b.

Watanabe, M. and Motoo, S., *Journal of Electroanalytical Chemistry*, 60, 267, 1975.

Watanabe, M., Uchida, M., and Motoo, S., *Journal of Electroanalytical Chemistry*, 229, 395, 1987.

Weeks, S.A., *Doctor of Philosophy Thesis, University of Oxford, U.K.*, 1988.

Williams, K. R., *An Introduction to Fuel Cells*, Elsevier, Amsterdam, 1966.

Yee, C., Scotti, M., Ulman, A., White, H., Rafailovich M., and Sokolov, J., *Langmuir*, 15, 4314, 1999.